ETH
Eidgenössische Technische Hochschule Zürich
Swiss Federal Institute of Technology Zurich

Seminar for Applied Mathematics SAM

Boundary Control in Computational Hemodynamics

T. Koltukluoğlu and P. Blanco

Research Report No. 2017-41
August 2017

Seminar für Angewandte Mathematik
Eidgenössische Technische Hochschule
CH-8092 Zürich
Switzerland

Boundary Control in Computational Hemodynamics

Taha S. Koltukluoğlu[1]† and Pablo J. Blanco[2]

[1]Seminar for Applied Mathematics, Swiss Federal Institute of Technology (ETH), Zürich, CH

[2]National Laboratory for Scientific Computing, (LNCC/MCTIC), Petrópolis, BR

(Received xx; revised xx; accepted xx)

In this work, a data assimilation method is proposed following an optimise-then-discretise approach, and is applied in the context of computational hemodynamics. The methodology aims to make use of phase-contrast magnetic resonance imaging to perform optimal flow control in computational fluid dynamic simulations. Flow matching between observations and model predictions is performed in luminal regions, excluding near-wall areas, improving the near-wall flow reconstruction to enhance the estimation of related quantities such as wall shear stresses. This work presents model validation against an analytical solution using the standard 3-D Hagen-Poiseuille flow, and validation with real data involving the flow control problem in a glass replica of a human aorta imaged with a 3T magnetic resonance scanner. The validation against in vitro experiments is performed for different flow regimes.

1. Introduction

Wall shear stresses (WSS) in arterial vessels have long been hypothesised to play a major role in the onset and progress of endothelial disorders. The dependence of endothelial cell function under different flow conditions and the impact of WSS in the development of atherosclerosis have been described in earlier studies (Texon *et al.* 1965; Ku *et al.* 1985; Zarins *et al.* 1987; Zand *et al.* 1991; Walpola *et al.* 1993; Malek *et al.* 1999). A brief review about underlying hypotheses for hemodynamic theories of atherogenesis was given by Gessner (1973). More recent studies explored the processes in the molecular, cellular and vascular levels, and supported the role of low WSS in the generation of coronary atherosclerosis and vascular remodelling (Chatzizisis *et al.* 2007; Chiu & Chien 2011). The effects of hemodynamics forces were discussed by Yoshida *et al.* (1990) considering the differences in biological fine structures of arterial walls in the human aorta and the endothelial morphology at bifurcations in rabbit aorta. Moreover, characterization of blood flow at and near the aortic wall plays an important role in the diagnosis of aortic aneurysms and their risk of rupture (Vorp *et al.* 1996; Vorp & Geest 2005).

Thus, the evaluation of shear stresses over the arterial wall, either using different computational strategies to simulate or to reconstruct blood flow, gained increasing interest in the cardiovascular research field. A basic approach to this problem consists of using data extracted from medical images to construct patient-specific vascular models and perform computational fluid dynamic (CFD) simulations of blood flow in these geometric models. The major drawback in such approaches lies in the lack of data to correctly set-up boundary conditions to the isolated arterial districts of interest. Rapidly,

† Email address for correspondence: ktaha@ethz.ch

the patient-specificity is lost when using generic criteria to prescribe such boundary conditions in CFD simulations.

A further step resides in using more advanced image acquisition techniques in an attempt to retrieve flow field measurements and merge them into the CFD simulations, thus providing more accurate patient-specific predictions. In this context, different methods exist to reconstruct the velocity field in a certain region of interest. Several works have already been reported addressing this problem using particle image velocimetry (PIV), ultrasound and 4-D phase-contrast magnetic resonance imaging (4-D flow MRI). A comprehensive review of several methods for flow reconstruction and the assessment of WSS is presented by Katritsis *et al.* (2007).

The use of PIV is known to be limited to in-vitro studies and cannot be applied to studying blood flow in in-vivo conditions (Hochareon *et al.* 2004). Differently, ultrasound imaging allows to extract 2-D information, thus requiring a 3-D flow reconstruction process, which is prone to lack accuracy in view of the incomplete nature of the data. Other limitation of ultrasound is that the WSS can only be estimated with acceptable accuracy in relatively straight arteries (Reneman *et al.* 2006). In turn, 4-D flow MRI offers the advantage of three-directional blood flow quantification with three-dimensional spatial encoding. Image reconstruction from the MRI data acquisition yields 3-D *CINE* magnitude images (anatomical data) and three phase difference images (velocity data), corresponding to the components of the 3-D velocity field. Moreover, MRI can be used in in-vivo scenarios noninvasively. Recent advances in MRI revealed a great diagnostic potential in hemodynamics applications (Markl *et al.* 2012; Kolipaka *et al.* 2016). Nevertheless, 4-D flow MRI also suffers from important limitations for the accurate quantification of blood flow in regions close to the arterial walls (near-wall regions), which is of the utmost importance for the patient-specific estimation of the WSS field. Due to the limited image resolution, acquired signals within the voxels at boundaries are obtained partially by the moving spins in the flowing blood and partially by the steady behavior of arterial tissue. This artifact is known as partial-volume-effect (Thang *et al.* 1995; Shaaban & Duerinckx 2000; Bouillot *et al.* 2017).

As a result of aforementioned advantages and limitations of imaging technologies, 4-D flow MRI procedures have become increasingly frequent in routine towards the improvement of CFD patient-specific simulations. However, the correct definition of the flow problem requires knowledge of initial and boundary conditions, as well as flow properties, i.e. blood density and blood viscosity. Particularly boundary conditions are usually not available, or cannot be measured accurately with current imaging techniques. Classical CFD methods (supported by MRI) usually apply fixed boundary conditions (BC) at the inlet of the arterial domain based on the noisy measurements extracted from the 4-D flow MRI data. This is why recent studies concentrated on optimal control strategies to alter BCs in such a way that the flow in the lumen matches the observations according to certain criteria. Optimal control supported by observations has been referred to as data assimilation (DA). Such studies were firstly and mainly applied in meteorology, physical oceanography and atmospheric flows (Council 1991; Ide *et al.* 1997). Owing to the shortcomings in the classical CFD approach (CFD employing noisy data as BCs), DA achieved an elevated attention in cardiovascular research field over the last decade.

Preliminary results of DA in tubular structures were reported by D'Elia & Veneziani (2010*a*) based on 2-D Stokes flow simulations. Convergence rate and noise sensitivity were investigated based on artificially generated noisy data. In D'Elia & Veneziani (2010*b*), their work was extended to the Oseen problem. Such strategy was employed in combination with a fixed point method to solve the Navier-Stokes, and perform flow matching in synthetically generated datasets using different mesh refinements. In

a further study, the authors extended their tests to an axis-symmetric cylinder and a 2-D geometry resembling a carotid artery (D'Elia *et al.* 2012). These studies were based on discretise-then-optimise (DO) approach, where the equations are first discretised and the optimisation is performed thereafter. Numerical results were mostly based on 2-D simplified geometries or on problems with rotational symmetry. These works were some of the first attempts to perform DA in blood flow simulations. However, real flow MRI measurements were not available in such studies.

In a recent work, DA was performed using more realistic vascular geometries (Tiago *et al.* 2016). First, a comparison between Dirichlet and Neumann boundary control was reported with the validation based on an idealised 2-D geometry with known solution. Secondly, numerical results were presented using a realistic 3-D geometry of a saccular brain aneurysm. The application of velocity control (Dirichlet BC) was claimed to recover the flow field better than the application of pressure control (Neumann BC). However, the flow data was synthetic and experiments with real 4-D flow MRI measurements were not available. Furthermore, they also applied the DO approach as a solution strategy. In (Collis & Heinkenschloss 2002), however, the authors concluded that the OD approach has better asymptotic convergence properties and leads to better adjoint approximations.

In this work, we propose a data assimilation method for 3-D steady state blood flow simulations following the optimise-then-discretise (OD) approach. To the authors' best knowledge, this is the first work performing an OD-based 3-D optimal flow control in the field of computational hemodynamics using true data acquisitions from 4-D flow MRI. The optimisation procedure is driven by the gradient of a given cost functional, computed within a variational framework. A Lagrangian method is employed for the calculation of the sensitivities from which the adjoint problem is derived. Further, the proposed approach considers cost functionals in the flow-matching formulation including the inlet and outlet boundaries (in addition to flow-matching in the volume of the domain). While previous studies mostly count on validations with known numerical solutions in simplified 2-D geometries, in this work we perform 3-D validation studies relying on an analytical solution based on the Hagen-Poiseuille flow. Additionally, we also present a sensitivity analysis with respect to changes in the optimisation parameters. Considering the noisy nature of 4-D flow MRI measurements, a universal outlier detection scheme is applied prior to the mapping of the flow field in the computational domain. Besides, a divergence-free space projection is employed to recover back the solenoidal property of measured flow field. An additional sensitivity analysis with respect to changes in the flow-matching domain is developed, which is important in determining the region-of-interest for the DA procedure. The optimisation solver was tested for different initial flow guesses demonstrating the sensitivity in the numerical results. Finally, the boundary flow control formulation and the preprocessing pipeline are combined to reconstruct the flow field in near-wall regions in a glass replica of the human aorta. For the latter, the methodology was tested for different flow regimes characterised by Reynolds (Re) numbers ranging from 1200 to 7100.

2. Mathematical Formulation

2.1. *Optimisation Problem*

Let us define a bounded Lipschitz domain $\Omega \subset \mathbb{R}^3$ along with its boundary $\partial\Omega = \Gamma_i \cup \Gamma_o \cup \Gamma_w$, where $\Gamma_i, \Gamma_o, \Gamma_w \subset \mathbb{R}^3$ stand for the inlet, outlet and arterial wall boundaries, respectively. Figure 1a illustrates such a domain resembling an aortic vascular geometry (to be used later in section 5). We further define a contracted subdomain $\Omega_s \subset \Omega$ with

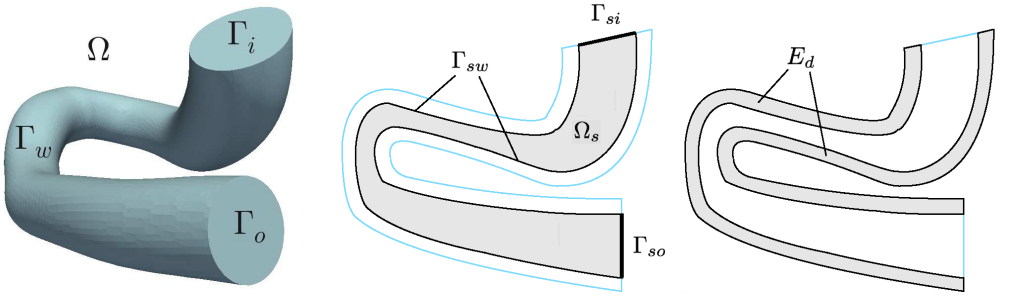

(a) (b) (c)

Figure 1: Computational domain. (a): Ω along with boundaries Γ_i : Inlet, Γ_o : Outlet and Γ_w : Wall. (b): Flow-matching domain $\Omega_s \subset \Omega$ with boundaries $\partial\Omega_s = \Gamma_{si} \cup \Gamma_{so} \cup \Gamma_{sw}$, which is at a distance s (mm) from Γ_w. (c): Error measurement domain E_d, which is within d (mm) distance from Γ_w.

boundary $\partial\Omega_s = \Gamma_{si} \cup \Gamma_{so} \cup \Gamma_{sw}$, where $\Gamma_{si} \subset \Gamma_i$ and $\Gamma_{so} \subset \Gamma_o$ (see figure 1b). The incompressible steady flow of a Newtonian fluid is considered in Ω. The inflow at Γ_i is prescribed by the function $\boldsymbol{g} = \boldsymbol{g}(\boldsymbol{x}) : \Gamma_i \to \mathbb{R}^3$, whereas the density and dynamic viscosity of the fluid are represented by ρ and μ, respectively. We highlight that the function $\boldsymbol{g}$ is such that $\boldsymbol{g}|_{\gamma_i} = 0$, where γ_i is the boundary of surface Γ_i. The blood flow velocity, $\boldsymbol{u} \in \boldsymbol{\mathcal{U}}^*$ with

$$\boldsymbol{\mathcal{U}}^* = \left\{ \boldsymbol{v} \in \boldsymbol{H}^1(\Omega) \mid \operatorname{div} \boldsymbol{v} = 0,\ \boldsymbol{v}|_{\Gamma_w} = \boldsymbol{0},\ \boldsymbol{v}|_{\Gamma_i} = \boldsymbol{g} \right\} \quad , \tag{2.1}$$

is solution of the steady state Navier-Stokes equations, which are written in variational form as follows:

$$\textit{Find } \boldsymbol{u} \in \boldsymbol{\mathcal{U}}^* \textit{ such that, } \int_\Omega \left[\rho(\nabla \boldsymbol{u})\boldsymbol{u} \cdot \hat{\boldsymbol{u}} + 2\mu \nabla^s \boldsymbol{u} \cdot \nabla^s \hat{\boldsymbol{u}} \right] d\Omega = 0 \quad \forall\, \hat{\boldsymbol{u}} \in \widehat{\boldsymbol{\mathcal{U}}}^* \quad , \tag{2.2}$$

where the strain rate tensor is defined as $\nabla^s(\cdot) = [\nabla(\cdot) + (\nabla(\cdot))^T]/2$, and

$$\widehat{\boldsymbol{\mathcal{U}}}^* = \left\{ \hat{\boldsymbol{v}} \in \boldsymbol{H}^1(\Omega) \mid \operatorname{div} \hat{\boldsymbol{v}} = 0,\ \hat{\boldsymbol{v}}|_{\Gamma_w} = \boldsymbol{0},\ \hat{\boldsymbol{v}}|_{\Gamma_i} = \boldsymbol{0} \right\} \quad . \tag{2.3}$$

The constraints $\operatorname{div} \boldsymbol{u} = 0$ and $\boldsymbol{u}|_{\Gamma_i} = \boldsymbol{g}$ can be relaxed using corresponding Lagrange multipliers p and $\boldsymbol{r}$. Now, introducing the space $\boldsymbol{\mathcal{U}} = \left\{ \boldsymbol{v} \in \boldsymbol{H}^1(\Omega) \mid \boldsymbol{v}|_{\Gamma_w} = \boldsymbol{0} \right\}$, problem (2.2) is equivalent to

$$\begin{aligned} &\mathscr{P}_\Omega : \textit{find } (\boldsymbol{u}, p, \boldsymbol{r}) \in \boldsymbol{\mathcal{U}} \times L^2(\Omega) \times \boldsymbol{H}^{-\frac{1}{2}}(\Gamma_i), \textit{ such that} \\ &\int_\Omega \left[\rho(\nabla \boldsymbol{u})\boldsymbol{u} \cdot \hat{\boldsymbol{u}} + 2\mu \nabla^s \boldsymbol{u} \cdot \nabla^s \hat{\boldsymbol{u}} - p \operatorname{div} \hat{\boldsymbol{u}} - \hat{p} \operatorname{div} \boldsymbol{u} \right] d\Omega \\ &= \int_{\Gamma_i} \hat{\boldsymbol{r}} \cdot (\boldsymbol{u} - \boldsymbol{g})\, d\Gamma + \int_{\Gamma_i} (\boldsymbol{r} \cdot \hat{\boldsymbol{u}})\, d\Gamma \quad \forall\, (\hat{\boldsymbol{u}}, \hat{p}, \hat{\boldsymbol{r}}) \in \boldsymbol{\mathcal{U}} \times L^2(\Omega) \times \boldsymbol{H}^{-\frac{1}{2}}(\Gamma_i) \quad . \end{aligned} \tag{2.4}$$

For the control flow problem, assume that some observations $\tilde{\boldsymbol{u}}^t \in \Omega$ are available. We want to find a velocity field $\boldsymbol{u}$, such that better matches the observations and, at the same time, is constrained to be a solution of Problem $\mathscr{P}_\Omega$. Based on a user-defined cost function, $\mathscr{O}$, such flow-matching problem can be cast as a mathematical optimisation problem, which reads

$$\mathscr{P}_M : \textit{ Find } \boldsymbol{g} \textit{ which minimises } \mathscr{O}(\boldsymbol{g}) = \mathscr{O}^*(\boldsymbol{u}(\boldsymbol{g}), \boldsymbol{g}, \tilde{\boldsymbol{u}}^t) \textit{ such that } \mathscr{P}_\Omega \textit{ holds, where}$$

$$\mathscr{O}(\boldsymbol{g}) = \frac{\alpha}{2}\left(\int_{\Omega_s}|\boldsymbol{u}(\boldsymbol{g})-\tilde{\boldsymbol{u}}^t|^2\,d\Omega + \int_{\Gamma_{si}}|\boldsymbol{u}(\boldsymbol{g})-\tilde{\boldsymbol{u}}^t|^2\,d\Gamma + \int_{\Gamma_{so}}|\boldsymbol{u}(\boldsymbol{g})-\tilde{\boldsymbol{u}}^t|^2\,d\Gamma\right) + \\ + \frac{\beta}{2}\int_{\Gamma_i}|\boldsymbol{g}|^2\,d\Gamma + \frac{\beta_1}{2}\int_{\Gamma_i}|\nabla_{\boldsymbol{\tau}}\,\boldsymbol{g}|^2\,d\Gamma\ . \tag{2.5}$$

2.2. *Optimality Conditions*

The flow-matching metric is defined on Ω_s, Γ_{si} and Γ_{so}, which are considered as the trust region of experimental observations (see figure 1b). Furthermore, $\nabla_{\boldsymbol{\tau}}$ denotes the surface gradient, and α, β and β_1 are user-defined parameters. To obtain the necessary optimality conditions for the optimisation problem $\mathscr{P}_M$, and to avoid the calculation of the derivative of the velocity field with respect to function $\boldsymbol{g}$, it is convenient to recast the problem of constrained optimisation as a saddle point problem. Correspondingly, we then construct the Lagrangian functional to relax the dependence of $\boldsymbol{u}$ from $\boldsymbol{g}$, as follows

$$\mathscr{L}(\boldsymbol{g},\boldsymbol{u},p,\boldsymbol{r},\boldsymbol{\lambda_u},\boldsymbol{\lambda}_p,\boldsymbol{\lambda_r}) = \mathscr{O}^*(\boldsymbol{u},\boldsymbol{g},\tilde{\boldsymbol{u}}^t) - \int_{\Gamma_i}\boldsymbol{\lambda_r}\cdot(\boldsymbol{u}-\boldsymbol{g})\,d\Gamma - \int_{\Gamma_i}\boldsymbol{r}\cdot\boldsymbol{\lambda_u}\,d\Gamma \\ + \int_{\Omega}\left[\rho(\nabla\boldsymbol{u})\boldsymbol{u}\cdot\boldsymbol{\lambda_u} + 2\mu\nabla^s\boldsymbol{u}\cdot\nabla^s\boldsymbol{\lambda_u} - p\,\mathrm{div}\,\boldsymbol{\lambda_u} - \lambda_p\,\mathrm{div}\,\boldsymbol{u}\right]d\Omega\ , \tag{2.6}$$

with $(\boldsymbol{g},\boldsymbol{u},p,\boldsymbol{r},\boldsymbol{\lambda_u},\lambda_p,\boldsymbol{\lambda_r}) \in \boldsymbol{H}_0^{\frac{1}{2}}(\Gamma_i)\times\boldsymbol{\mathcal{U}}\times L^2(\Omega)\times\boldsymbol{H}^{-\frac{1}{2}}(\Gamma_i)\times\boldsymbol{\mathcal{U}}\times L^2(\Omega)\times\boldsymbol{H}^{-\frac{1}{2}}(\Gamma_i)$. Further, let us consider the perturbations $\hat{(\cdot)}$ to the fields $(\cdot)$ above, as $(\cdot)+\tau\hat{(\cdot)}$, that is

$$\boldsymbol{g}\to\boldsymbol{g}+\tau\hat{\boldsymbol{g}} \qquad \boldsymbol{g},\hat{\boldsymbol{g}}\in\boldsymbol{H}_0^{\frac{1}{2}}(\Gamma_i)\ , \tag{2.7}$$
$$\boldsymbol{u}\to\boldsymbol{u}+\tau\hat{\boldsymbol{u}} \qquad \boldsymbol{u},\hat{\boldsymbol{u}}\in\boldsymbol{\mathcal{U}}\ , \tag{2.8}$$
$$p\to p+\tau\hat{p} \qquad p,\hat{p}\in L^2(\Omega)\ , \tag{2.9}$$
$$\boldsymbol{r}\to\boldsymbol{r}+\tau\hat{\boldsymbol{r}} \qquad \boldsymbol{r},\hat{\boldsymbol{r}}\in\boldsymbol{H}^{-\frac{1}{2}}(\Gamma_i)\ , \tag{2.10}$$
$$\boldsymbol{\lambda_u}\to\boldsymbol{\lambda_u}+\tau\hat{\boldsymbol{\lambda}}_{\boldsymbol{u}} \qquad \boldsymbol{\lambda_u},\hat{\boldsymbol{\lambda}}_{\boldsymbol{u}}\in\boldsymbol{\mathcal{U}}\ , \tag{2.11}$$
$$\lambda_p\to\lambda_p+\tau\hat{\lambda}_p \qquad \lambda_p,\hat{\lambda}_p\in L^2(\Omega)\ , \tag{2.12}$$
$$\boldsymbol{\lambda_r}\to\boldsymbol{\lambda_r}+\tau\hat{\boldsymbol{\lambda}}_{\boldsymbol{r}} \qquad \boldsymbol{\lambda_r},\hat{\boldsymbol{\lambda}}_{\boldsymbol{r}}\in\boldsymbol{H}^{-\frac{1}{2}}(\Gamma_i)\ , \tag{2.13}$$

where $\boldsymbol{H}_0^{1/2}(\Gamma_i)$ is the space of traces over Γ_i of $\boldsymbol{H}^1(\Omega)$ functions which are zero over γ_i, the boundary of surface Γ_i. The Gâteaux derivative of the Lagrangian functional is denoted as follows

$$\left\langle\frac{\partial\mathscr{L}}{\partial a},\hat{a}\right\rangle = \frac{d}{d\tau}\mathscr{L}(\ldots,a+\tau\hat{a},\ldots)\bigg|_{\tau=0}\ . \tag{2.14}$$

Our goal is to compute the Gâteaux derivative of $\mathscr{O}$ with respect to perturbation in $\boldsymbol{g}$,

$$\left\langle\frac{\partial\mathscr{O}}{\partial\boldsymbol{g}},\hat{\boldsymbol{g}}\right\rangle = \frac{d}{d\tau}\mathscr{O}(\boldsymbol{g}+\tau\hat{\boldsymbol{g}})\bigg|_{\tau=0}\ . \tag{2.15}$$

The critical points of the Lagrangian (2.6) contain information on the aforementioned Gâteaux derivative (2.15), and are characterised by

$$\left\langle\frac{\partial\mathscr{L}}{\partial(\boldsymbol{\lambda_u},\boldsymbol{\lambda}_p,\boldsymbol{\lambda_r})},\begin{pmatrix}\hat{\boldsymbol{\lambda}}_{\boldsymbol{u}}\\ \hat{\boldsymbol{\lambda}}_p\\ \hat{\boldsymbol{\lambda}}_{\boldsymbol{r}}\end{pmatrix}\right\rangle = \boldsymbol{0}\ ,\quad \left\langle\frac{\partial\mathscr{L}}{\partial(\boldsymbol{u},p,\boldsymbol{r})},\begin{pmatrix}\hat{\boldsymbol{u}}\\ \hat{p}\\ \hat{\boldsymbol{r}}\end{pmatrix}\right\rangle = \boldsymbol{0}\ ,\quad \left\langle\frac{\partial\mathscr{L}}{\partial\boldsymbol{g}},\hat{\boldsymbol{g}}\right\rangle = 0\ . \tag{2.16}$$

The first and second equations in (2.16) describe the direct and the so-called adjoint equations to solve for the state variables $(\boldsymbol{u},p,\boldsymbol{r})$ and the adjoint variables $(\boldsymbol{\lambda_u},\boldsymbol{\lambda}_p,\boldsymbol{\lambda_r})$,

respectively. Finally, the last equation in (2.16) provides the optimality condition of cost functional with respect to perturbations in $\boldsymbol{g}$. Particularly, it also follows that

$$\left\langle \frac{\partial \mathscr{O}}{\partial \boldsymbol{g}}, \hat{\boldsymbol{g}} \right\rangle = \left\langle \frac{\partial \mathscr{L}}{\partial \boldsymbol{g}}, \hat{\boldsymbol{g}} \right\rangle \Bigg|_{\substack{(\boldsymbol{u},p,\boldsymbol{r}) \text{ solution of direct problem} \\ (\boldsymbol{\lambda_u},\lambda_p,\boldsymbol{\lambda_r}) \text{ solution of adjoint problem}}} . \tag{2.17}$$

Let us now compute the Gâteaux derivatives (2.16). We first obtain the direct problem by taking the derivative with respect to the variables $(\boldsymbol{\lambda_u}, \lambda_p, \boldsymbol{\lambda_r})$. Then, the following problem is obtained:

$\mathscr{P}_{\text{sta}}(\boldsymbol{g})$: *For* $\boldsymbol{g} \in \boldsymbol{H}_0^{\frac{1}{2}}(\Gamma_i)$, *determine* $(\boldsymbol{u}, p, \boldsymbol{r}) \in \boldsymbol{\mathcal{U}} \times L^2(\Omega) \times \boldsymbol{H}^{-\frac{1}{2}}(\Gamma_i)$ *such that*

$$\left\langle \frac{\partial \mathscr{L}}{\partial \boldsymbol{\lambda_u}}, \hat{\boldsymbol{\lambda}}_{\boldsymbol{u}} \right\rangle = \int_\Omega \left[\rho(\nabla \boldsymbol{u})\boldsymbol{u} \cdot \hat{\boldsymbol{\lambda}}_{\boldsymbol{u}} + 2\mu \nabla^s \boldsymbol{u} \cdot \nabla^s \hat{\boldsymbol{\lambda}}_{\boldsymbol{u}} - p \operatorname{div} \hat{\boldsymbol{\lambda}}_{\boldsymbol{u}} \right] d\Omega - \int_{\Gamma_i} \boldsymbol{r} \cdot \hat{\boldsymbol{\lambda}}_{\boldsymbol{u}} \, d\Gamma = 0 \qquad \forall\, \hat{\boldsymbol{\lambda}}_{\boldsymbol{u}} \in \boldsymbol{\mathcal{U}} \ , \tag{2.18}$$

$$\left\langle \frac{\partial \mathscr{L}}{\partial \lambda_p}, \hat{\lambda}_p \right\rangle = - \int_\Omega \hat{\lambda}_p \operatorname{div} \boldsymbol{u} \, d\Omega = 0 \qquad \forall\, \hat{\lambda}_p \in L^2(\Omega) \ , \tag{2.19}$$

$$\left\langle \frac{\partial \mathscr{L}}{\partial \boldsymbol{\lambda_r}}, \hat{\boldsymbol{\lambda}}_{\boldsymbol{r}} \right\rangle = - \int_{\Gamma_i} \hat{\boldsymbol{\lambda}}_{\boldsymbol{r}} \cdot (\boldsymbol{u} - \boldsymbol{g}) \, d\Gamma = 0 \qquad \forall\, \hat{\boldsymbol{\lambda}}_{\boldsymbol{r}} \in \boldsymbol{H}^{-\frac{1}{2}}(\Gamma_i) \ . \tag{2.20}$$

The Euler-Lagrange equations associated to (2.18)-(2.19)-(2.20) are the classical Navier-Stokes equations, which read as follows

$$\rho(\nabla \boldsymbol{u})\boldsymbol{u} - \mu \Delta \boldsymbol{u} + \nabla p = \boldsymbol{0} \qquad \text{in } \Omega \ , \tag{2.21}$$

$$\operatorname{div} \boldsymbol{u} = 0 \qquad \text{in } \Omega \ , \tag{2.22}$$

$$\boldsymbol{u} = \boldsymbol{0} \qquad \text{on } \Gamma_w \ , \tag{2.23}$$

$$\boldsymbol{u} = \boldsymbol{g} \qquad \text{on } \Gamma_i \ , \tag{2.24}$$

$$(-p\boldsymbol{I} + 2\mu \nabla^s \boldsymbol{u})\boldsymbol{n} = \boldsymbol{r} \qquad \text{on } \Gamma_i \ , \tag{2.25}$$

$$(-p\boldsymbol{I} + 2\mu \nabla^s \boldsymbol{u})\boldsymbol{n} = \boldsymbol{0} \qquad \text{on } \Gamma_o \ . \tag{2.26}$$

Secondly, we obtain the adjoint problem by taking the derivative of Lagrangian (2.6) with respect to state variables $(\boldsymbol{u}, p, \boldsymbol{r})$. The adjoint problem then reads as

$\mathscr{P}_{\text{adj}}(\boldsymbol{u}, \tilde{\boldsymbol{u}}^t)$: *For* $\tilde{\boldsymbol{u}}^t$, and $\boldsymbol{u}$, solution of (2.21)–(2.26),

determine $(\boldsymbol{\lambda_u}, \lambda_p, \boldsymbol{\lambda_r}) \in \boldsymbol{\mathcal{U}} \times L^2(\Omega) \times \boldsymbol{H}^{-\frac{1}{2}}(\Gamma_i)$, *such that*

$$\left\langle \frac{\partial \mathscr{L}}{\partial \boldsymbol{u}}, \hat{\boldsymbol{u}} \right\rangle = \int_{\Gamma_o \cup \Gamma_i} \left[\alpha \, (\chi_{\Gamma_{so}} + \chi_{\Gamma_{si}})(\boldsymbol{u} - \tilde{\boldsymbol{u}}^t) \cdot \hat{\boldsymbol{u}} \right] d\Gamma - \int_{\Gamma_i} \left(\boldsymbol{\lambda_r} \cdot \hat{\boldsymbol{u}} \right) d\Gamma + \int_\Omega \Big[\alpha \, \chi_{\Omega_s} (\boldsymbol{u} - \tilde{\boldsymbol{u}}^t) \cdot \hat{\boldsymbol{u}} + \rho(\nabla \hat{\boldsymbol{u}})\boldsymbol{u} \cdot \boldsymbol{\lambda_u} + \rho(\nabla \boldsymbol{u})\hat{\boldsymbol{u}} \cdot \boldsymbol{\lambda_u} + + 2\mu \nabla^s \hat{\boldsymbol{u}} \cdot \nabla^s \boldsymbol{\lambda_u} - \lambda_p \operatorname{div} \hat{\boldsymbol{u}} \Big] d\Omega = 0 \qquad \forall\, \hat{\boldsymbol{u}} \in \boldsymbol{\mathcal{U}} \ , \tag{2.27}$$

$$\left\langle \frac{\partial \mathscr{L}}{\partial p}, \hat{p} \right\rangle = - \int_\Omega \hat{p} \operatorname{div} \boldsymbol{\lambda_u} \, d\Omega = 0 \qquad \forall\, \hat{p} \in L^2(\Omega) \ , \tag{2.28}$$

$$\left\langle \frac{\partial \mathscr{L}}{\partial \boldsymbol{r}}, \hat{\boldsymbol{r}} \right\rangle = - \int_{\Gamma_i} \hat{\boldsymbol{r}} \cdot \boldsymbol{\lambda_u} \, d\Gamma = 0 \qquad \forall\, \hat{\boldsymbol{r}} \in \boldsymbol{H}^{-\frac{1}{2}}(\Gamma_i) \ , \tag{2.29}$$

where, we considered the following indicator functions,

$$\chi_{\Omega_s} = \begin{cases} 1 & \text{in } \Omega_s \ , \\ 0 & \text{in } \Omega \setminus \Omega_s \ , \end{cases} \qquad \chi_{\Gamma_{si}} = \begin{cases} 1 & \text{in } \Gamma_{si} \ , \\ 0 & \text{in } \Gamma_i \setminus \Gamma_{si} \ , \end{cases} \qquad \chi_{\Gamma_{so}} = \begin{cases} 1 & \text{in } \Gamma_{so} \ , \\ 0 & \text{in } \Gamma_o \setminus \Gamma_{so} \ . \end{cases} \tag{2.30}$$

Applying standard variational arguments for (2.27)-(2.28)-(2.29) delivers the associated Euler-Lagrange equations, as follows

$$\alpha\,\chi_{\Omega_s}(\boldsymbol{u}-\tilde{\boldsymbol{u}}^t)-\rho(\nabla\boldsymbol{\lambda_u})\boldsymbol{u}+\rho(\nabla\boldsymbol{u})^T\boldsymbol{\lambda_u}-\mu\Delta\boldsymbol{\lambda_u}+\nabla\lambda_p=\boldsymbol{0}\qquad\text{in }\Omega\ , \tag{2.31}$$

$$\operatorname{div}\boldsymbol{\lambda_u}=0\qquad\text{in }\Omega\ , \tag{2.32}$$

$$\boldsymbol{\lambda_u}=\boldsymbol{0}\qquad\text{on }\Gamma_w\ , \tag{2.33}$$

$$\boldsymbol{\lambda_u}=\boldsymbol{0}\qquad\text{on }\Gamma_i\ , \tag{2.34}$$

$$\alpha\,\chi_{\Gamma_{si}}(\boldsymbol{u}-\tilde{\boldsymbol{u}}^t)+(-\lambda_p\boldsymbol{I}+2\mu\nabla^s\boldsymbol{\lambda_u})\boldsymbol{n}=\boldsymbol{\lambda_r}\qquad\text{on }\Gamma_i\ , \tag{2.35}$$

$$\alpha\,\chi_{\Gamma_{so}}(\boldsymbol{u}-\tilde{\boldsymbol{u}}^t)+\rho(\boldsymbol{u}\cdot\boldsymbol{n})\boldsymbol{\lambda_u}+(-\lambda_p\boldsymbol{I}+2\mu\nabla^s\boldsymbol{\lambda_u})\boldsymbol{n}=\boldsymbol{0}\qquad\text{on }\Gamma_o\ . \tag{2.36}$$

Finally, let us compute the optimality condition, which states

$\mathscr{P}_{\rm opt}(\boldsymbol{\lambda_r})$: *For* $\boldsymbol{\lambda_r}$, *solution of* (2.31)–(2.36), *determine* $\boldsymbol{g}\in\boldsymbol{H}_0^{\frac{1}{2}}(\Gamma_i)$, *such that*

$$\left\langle\frac{\partial\mathscr{L}}{\partial\boldsymbol{g}},\hat{\boldsymbol{g}}\right\rangle=\int_{\Gamma_i}\left[\beta\boldsymbol{g}\cdot\hat{\boldsymbol{g}}+\beta_1\nabla_{\boldsymbol{\tau}}\boldsymbol{g}\cdot\nabla_{\boldsymbol{\tau}}\hat{\boldsymbol{g}}+\boldsymbol{\lambda_r}\cdot\hat{\boldsymbol{g}}\right]d\Gamma=0\quad\forall\,\hat{\boldsymbol{g}}\in\boldsymbol{H}^{\frac{1}{2}}(\Gamma_i)\ . \tag{2.37}$$

The Euler-Lagrange equations associated to (2.37) are the following,

$$\beta\boldsymbol{g}-\beta_1\triangle_{\boldsymbol{\tau}}\boldsymbol{g}=-\boldsymbol{\lambda_r}\qquad\text{on }\Gamma_i\ , \tag{2.38}$$

$$\boldsymbol{g}=\boldsymbol{0}\qquad\text{on }\gamma_i\ , \tag{2.39}$$

where $\boldsymbol{\lambda_r}$ is solution of the adjoint problem $\mathscr{P}_{\rm adj}$.

2.3. *Gradient Descent Algorithm*

The procedure to solve the optimality conditions at once amounts to solve the nonlinear system of coupled variational equations $\mathscr{P}_{\rm sta}$, $\mathscr{P}_{\rm adj}$ and $\mathscr{P}_{\rm opt}$ (or their corresponding Euler-Lagrange equations (2.21)–(2.26), (2.31)–(2.36) and (2.38)–(2.39)). This problem is highly nonlinear and a possible way to find the stationary point for the optimisation problem $\mathscr{P}_M$ is to evaluate the Gâteaux derivative (2.17) to drive a descent-like iterative algorithm. In this case, first, given a guess $\boldsymbol{g}$, the forward problem, $\mathscr{P}_{\rm sta}$, is solved to obtain the state variables, $(\boldsymbol{u},p,\boldsymbol{r})$. Second, the adjoint problem, $\mathscr{P}_{\rm adj}$, is evaluated using the solution, $\boldsymbol{u}$, from the direct problem. Then, using the adjoint variable, $\boldsymbol{\lambda_r}$, obtained from the adjoint problem, the gradient of the objective function with respect to the parameter $\boldsymbol{g}$ can be calculated from (2.37), as follows,

$$\frac{D\mathscr{O}(\boldsymbol{g})}{D\boldsymbol{g}}=\beta\boldsymbol{g}-\beta_1\triangle_{\boldsymbol{\tau}}\boldsymbol{g}+\boldsymbol{\lambda_r}\quad\text{on }\Gamma_i\ . \tag{2.40}$$

To ensure an acceptable, converging solution of the algorithm, it is usual to start with solving the forward problem based on some initial guess, $(\boldsymbol{u})_0$, for the flow field. Therefore, we introduce a proper linearisation, $\mathscr{P}_{\rm sta}^{\rm lin}$, of the forward problem, $\mathscr{P}_{\rm sta}$, as

$\mathscr{P}_{\rm sta}^{\rm lin}(\boldsymbol{u}^*,\boldsymbol{g}^*)$: *For* $\boldsymbol{u}^*$ *and* $\boldsymbol{g}^*$, *determine* $(\boldsymbol{u},p,\boldsymbol{r})$ *such that*

$$\begin{aligned}&\int_\Omega\left[\rho(\nabla\boldsymbol{u})\boldsymbol{u}^*\cdot\hat{\boldsymbol{\lambda}}_{\boldsymbol{u}}+2\mu\nabla^s\boldsymbol{u}\cdot\nabla^s\hat{\boldsymbol{\lambda}}_{\boldsymbol{u}}-p\operatorname{div}\hat{\boldsymbol{\lambda}}_{\boldsymbol{u}}\right]d\Omega-\\&-\int_{\Gamma_i}\boldsymbol{r}\cdot\hat{\boldsymbol{\lambda}}_{\boldsymbol{u}}\,d\Gamma=0\qquad\forall\,\hat{\boldsymbol{\lambda}}_{\boldsymbol{u}}\in\boldsymbol{\mathcal{U}}\ ,\\&-\int_\Omega\hat{\lambda}_p\operatorname{div}\boldsymbol{u}\,d\Omega=0\qquad\forall\,\hat{\lambda}_p\in L^2(\Omega)\ ,\\&-\int_{\Gamma_i}\hat{\boldsymbol{\lambda}}_{\boldsymbol{r}}\cdot(\boldsymbol{u}-\boldsymbol{g}^*)\,d\Gamma=0\qquad\forall\,\hat{\boldsymbol{\lambda}}_{\boldsymbol{r}}\in\boldsymbol{H}^{-\frac{1}{2}}(\Gamma_i)\ .\end{aligned} \tag{2.41}$$

The optimality condition, (2.37), ensures that the derivative of the objective functional with respect to the control parameters vanishes at the critical point. In the gradient descent algorithm, however, the optimality condition is not satisfied until the algorithm converges. That procedure is described in algorithm 1 below. The fields $(\cdot)^k$ correspond to the fields $(\cdot)$ at k-th iteration. Parameter σ represents the step size, which is adjusted dynamically. To test convergence, a small parameter ξ is prescribed as a tolerance to potentially exit the algorithm, if necessary.

Algorithm 1 Steepest descent with dynamic step size

Given: $\alpha, \beta, \beta_1 > 0$ ▷ Set optimisation parameters
Input : $\boldsymbol{u}^0, \boldsymbol{g}^0, \tilde{\boldsymbol{u}}^t$ ▷ Provide initial guess and target flow
Output : $\boldsymbol{u}^k$ ▷ Flow field at last iteration k

procedure DataAssimilation($\boldsymbol{u}^0, \boldsymbol{g}^0, \tilde{\boldsymbol{u}}^t$)
  $\sigma \leftarrow 1$, $\xi \leftarrow 10^{-8}$ and $k \leftarrow 0$
  $(\boldsymbol{u}^0, \cdot, \cdot) \leftarrow \mathscr{P}^{\text{lin}}_{\text{sta}}(\boldsymbol{u}^0, \boldsymbol{g}^0)$ ▷ Evaluate linearised problem (2.41)
  $cost^0 \leftarrow \mathscr{O}^*(\boldsymbol{u}^0, \boldsymbol{g}^0, \tilde{\boldsymbol{u}}^t)$ ▷ Evaluate cost function (2.5)
  for $k \leftarrow 1, n$ **do**
    $(\cdot, \cdot, \boldsymbol{\lambda}^k_{\boldsymbol{r}}) \leftarrow \mathscr{P}_{\text{adj}}(\boldsymbol{u}^{k-1}, \tilde{\boldsymbol{u}}^t)$ ▷ Evaluate adjoint problem (2.27)–(2.29)
    $\boldsymbol{s}^k \leftarrow -(\beta \boldsymbol{g}^{k-1} - \beta_1 \triangle_{\boldsymbol{r}} \boldsymbol{g}^{k-1} + \boldsymbol{\lambda}^k_{\boldsymbol{r}})$ ▷ Set steepest descent direction (2.40)
    repeat
      $\boldsymbol{g}^k \leftarrow \boldsymbol{g}^{k-1} + \sigma \boldsymbol{s}^k$ ▷ Update control, using step size σ
      $(\boldsymbol{u}^k, \cdot, \cdot) \leftarrow \mathscr{P}^{\text{lin}}_{\text{sta}}(\boldsymbol{u}^{k-1}, \boldsymbol{g}^k)$
      $cost^k \leftarrow \mathscr{O}^*(\boldsymbol{u}^k, \boldsymbol{g}^k, \tilde{\boldsymbol{u}}^t)$
      if $cost^k \geqslant cost^{k-1}$ **then**
        $\sigma \leftarrow 0.5\sigma$
      end if
    until $cost^k < cost^{k-1}$
    if $(|cost^k - cost^{k-1}|)/(cost^k) > \xi$ **then**
      $\sigma \leftarrow 1.5\sigma$
    else
      return $\boldsymbol{u}^k$
    end if
  end for
end procedure

2.4. *Numerical Methods*

The direct and adjoint problems were approximated using the finite volume method. The linearised problem, $\mathscr{P}^{\text{lin}}_{\text{sta}}$, was solved using the SIMPLE algorithm described by Patankar & Spalding (1972). According to this, the momentum equation (2.21) is solved (after proper linearisation and discretisation) starting with an initial guess for pressure. In addition, a pressure correction equation is derived from the continuity equation (2.21) obtaining the pressure correction field, which is then used to update both the pressure and the velocity. To solve the discretised momentum equation, we applied the Gauss-

Seidel method. Then, the discretised pressure correction equation was solved using a generalised geometric-algebraic multi-grid (GAMG) solver using Gauss-Seidel iterations. The adjoint equations (2.31)–(2.36) were discretised and solved in a similar way, following the SIMPLE algorithm and using the same solvers as described for the solution of the direct problem. That is, Gauss-Seidel iterations were used to solve the adjoint momentum equation (2.31) (after its corresponding discretisation) and GAMG was used for solving the discretised adjoint pressure correction derived from the adjoint continuity equation (2.32). The entire optimisation algorithm including the direct and adjoint solvers were implemented using the open source CFD library, OpenFOAM (Weller *et al.* 1998).

3. Preprocessing of Observational Data

The proposed approach was validated and tested based on data, which were generated both artificially and empirically. Generated artificial data were used to validate the approach on a simplified geometry, where analytical solutions are available (see section 4). The experimental data were generated with MRI measurements acquired for a glass replica of a human aorta (see section 5). Both kinds of observations contain either some artificially added or realistic noise, respectively. Hence, the data further requires some preprocessing, prior to the application of the proposed optimisation algorithm. Let $\boldsymbol{u}_{\mathbf{mri}}$ denote the noisy data, which is either artificially generated or obtained from the MR scan. First of all, a noise detection strategy was applied to the observed data, $\boldsymbol{u}_{\mathbf{mri}}$, to eliminate potential spurious vectors, yielding a denoised flow field, $\boldsymbol{u}^{\circ}_{\mathbf{mri}}$. Secondly, the vascular domain was segmented from (either artificial or experimental) MRI data and was registered with the exact phantom geometry (for the experimental scenario). For both artificial and experimental data, the geometries were available as either a user-generated cylinder or the surface data representing the 3-D print of glass replica, respectively. Furthermore, the computational mesh was created from such exact geometries. The measured and denoised velocity field, $\boldsymbol{u}^{\circ}_{\mathbf{mri}}$, inside the segmented region of interest were mapped into the computational mesh domain, using the transformation obtained from the registration step. This mapping was performed using linear interpolation, yielding a denoised flow field in the computational mesh domain denoted as $\bar{\boldsymbol{u}}_{\mathbf{mri}}$. Finally, a space projection was applied to $\bar{\boldsymbol{u}}_{\mathbf{mri}}$ to recover back the divergence-free property of the flow data, which returns a flow field called $\tilde{\boldsymbol{u}}^{\star}$. The preprocessing steps can be tabularly summarised as follows:

$$\boldsymbol{u}_{\mathbf{mri}} \xrightarrow{\text{Outlier Detection}} \boldsymbol{u}^{\circ}_{\mathbf{mri}} \xrightarrow{\text{Registration}} \bar{\boldsymbol{u}}_{\mathbf{mri}} \xrightarrow{\text{Space Projection}} \tilde{\boldsymbol{u}}^{\star}$$

$\boldsymbol{u}_{\mathbf{mri}}$: Reconstructed flow field from 4-D flow MRI (or artificially generated),

$\boldsymbol{u}^{\circ}_{\mathbf{mri}}$: Denoised flow field defined in observational domain (usually coarse mesh),

$\bar{\boldsymbol{u}}_{\mathbf{mri}}$: Linearly interpolated flow field mapped in the computational domain (fine mesh),

$\tilde{\boldsymbol{u}}^{\star}$: Divergence-free flow field defined in the computational domain.

3.1. *Noise Detection*

A variation of the usual median test, proposed by Westerweel & Scarano (2005) and initially applied to PIV, was implemented and applied to MRI data, $\boldsymbol{u}_{\mathbf{mri}}$, for detecting the spurious vectors in the measurements. The method utilises a normalization to the original median test and considers the local fluctuations of the flow field. For a wide variety of documented flow cases, Westerweel and Scarano verified the generality of the method for Re numbers ranging from 10^{-1} to 10^{7}.

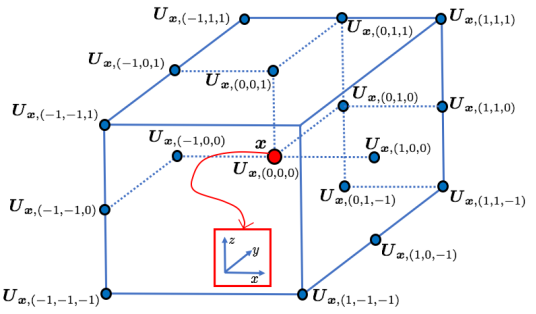

Figure 2: For $R = 1$, the set $\boldsymbol{U}_{\boldsymbol{x},N_1}$ is shown with the 26 neighbours of $\boldsymbol{U}_{\boldsymbol{x}}$ (not all neighbours illustrated). Note that N_R does not contain the tuple $(0,0,0)$, hence $\boldsymbol{U}_{\boldsymbol{x}} = \boldsymbol{U}_{\boldsymbol{x},(0,0,0)}$ is not included in $\boldsymbol{U}_{\boldsymbol{x},N_1}$.

For a more formal description of the method, let us first introduce a set of 3-tuples,

$$N_R = \{\,(i,j,k) \in \mathbb{Z} \mid -R \leqslant i,j,k \leqslant R \wedge R \in \mathbb{N}\,\} \setminus \{\,(0,0,0)\,\} \quad . \tag{3.1}$$

Secondly, we define $\boldsymbol{U}_{\boldsymbol{x}} = \boldsymbol{U}_{\boldsymbol{x},(0,0,0)} \in \mathbb{R}^n$ to be the displacement vector at pixel position $\boldsymbol{x}$ and $\boldsymbol{U}_{\boldsymbol{x},N_R}$ is the set of its $[(2R+1)^3 - 1]$ neighbours. Figure 2 illustrates the neighborhood for $R = 1$. Additionally, let $\boldsymbol{U}_{\boldsymbol{x},\mathrm{med}}$ be the median of $\boldsymbol{U}_{\boldsymbol{x},N_R}$. The classical median test value is defined as $(\mathrm{MT})_{\boldsymbol{x},N_R} = \|\boldsymbol{U}_{\boldsymbol{x},\mathrm{med}} - \boldsymbol{U}_{\boldsymbol{x}}\|$, which is passed if it is smaller than a user defined threshold value ϵ_t. Furthermore, we define the set of residuals, $r_{\boldsymbol{x},N_R}$, as

$$r_{\boldsymbol{x},N_R} = \{\, r \in \mathbb{R} \mid r = \|\boldsymbol{U} - \boldsymbol{U}_{\boldsymbol{x},\mathrm{med}}\| \wedge \boldsymbol{U} \in \boldsymbol{U}_{\boldsymbol{x},N_R} \,\} \quad , \tag{3.2}$$

and similarly, $r_{\boldsymbol{x},\mathrm{med}}$ is defined to be the median of $r_{\boldsymbol{x},N_R}$, which is used to normalise the usual median test:

$$(\mathrm{NMT})_{\boldsymbol{x},N_R} = \frac{\|\boldsymbol{U}_{\boldsymbol{x},\mathrm{med}} - \boldsymbol{U}_{\boldsymbol{x}}\|}{r_{\boldsymbol{x},\mathrm{med}} + \epsilon} < \epsilon_t \quad . \tag{3.3}$$

Under uniform flow conditions the main normalization factor $r_{\boldsymbol{x},\mathrm{med}}$ tends to yield zero, hence a small and acceptable local fluctuation level ϵ is applied to compensate for a potential division by zero and to account for remaining velocity fluctuations obtained from cross correlation analysis. In practice, ϵ values between 0.1 and 0.2 might be used (Westerweel & Scarano 2005; Raffel *et al.* 2007; Garcia 2011). In our case, $\epsilon = 0.2$ performed well for the available MR flow data. Furthermore, $\epsilon_t = 2.25$ is used as validation threshold. Once the latter parameter is detected from numerical experiments, it can be used for other data at similar flow regimes with the same imaging modality.

Prior to the application of noise detection, the observations, $\boldsymbol{u}_{\mathbf{mri}}$, obtained from MRI measurements are initially already divergence-free. This is ensured by the constraints applied during the reconstruction process of MRI data, which is out of scope of this work. After denoising, however, the detected spurious vectors are erased from the data which results in a flow field $\boldsymbol{u}^{\circ}_{\mathbf{mri}}$ with gaps at certain positions within the observations. This clearly violates the divergence-free property of observed data, $\boldsymbol{u}_{\mathbf{mri}}$. One possible way to fill in the gaps would be the use of some interpolation scheme. However, such schemes will not necessarily ensure a solenoidal flow field. Therefore, we rely on the application of a projection over a divergence-free space at a later stage (see section 3.4) to automatically fill in the aforementioned gaps and to recover back the divergence-free property of the flow field.

3.2. *Segmentation and Registration*

After the removal of outliers, the arterial structures, in which the analysis is to be performed, are segmented from both the artificially generated flow data as well as from the acquired MR measurements. The artificial data consists only in the flow field generated in a cylindrical geometry, whereas the experimental MRI data comprises the anatomical structures and the velocity field data (Markl *et al.* 2012). For validation studies, the flow data were used for segmentation of the cylindrical geometry (see section 4), whereas for experimental studies, the anatomical data from MR images were used to extract the vascular geometry from the aorta replica (see section 5). The segmentation was performed using the snake evolution method available in ITK-SNAP (www.itksnap.org) and was smoothed using the tools available in the VMTK library (www.vmtk.org).

For the comparison with experimental MRI data, a high resolution aortic surface data was already available from the 3-D print of glass replica. The latter was used to generate the computational mesh for the exact geometry. However, after image acquisition and segmentation, the flow data is misaligned with the exact geometry of replica. Therefore, a registration step was necessary to align the measured flow field with the exact geometry of replica. The rigid registration was performed using ITK point-set to point-set method (www.itk.org). In the case of the artificially generated flow data in the cylindrical domain, no further registration step was required, since the geometry was already aligned with the segmented domain.

3.3. *Mapping in the Computational Mesh*

For both cases, the analytical geometry (cylinder) and the experimental geometry (glass replica of aorta), the available exact geometries were used to generate the computational mesh domain, which is used for the flow simulations. For both datasets, a hexahedral mesh was created using OpenFOAM's snappyHexMesh procedure. In the case of experimental geometry, the mesh was rigidly transformed into its corresponding segmentation using the mapping obtained from the registration step. After mesh generation, the velocities, $\boldsymbol{u}^{\circ}_{\mathbf{mri}}$, from the denoised phase difference images (obtained from 4-D flow MRI and denoised with the universal outlier detection scheme) with limited resolution (i.e. in a coarse observational domain) were mapped into the fine hexahedral mesh (computational domain for CFD simulations with high resolution) using the linear interpolation method available in ITK (Johnson *et al.* 2013). As a result of the combination of the linear interpolation and the previous noise detection process, the final flow field (denoted by $\bar{\boldsymbol{u}}_{\mathbf{mri}}$) in the CFD mesh is not divergence-free. The divergence-free property is then recovered with the projection over a divergence-free space applied to the velocity field in the CFD mesh as explained next.

3.4. *Projection into Divergence-Free Space*

Let $\bar{\boldsymbol{u}}_{\mathbf{mri}} \in \left(L^2\left(\Omega\right)\right)^3$ be a given observation, projected in a bounded Lipschitz domain $\Omega \in \mathbb{R}^3$ with boundary $\partial\Omega$. According to Helmholtz-Hodge decomposition (HHD), the velocity field can be decomposed into the sum of its divergence-free, curl-free and gradient of harmonic components, if the fluid velocity is known at the boundary (Denaro 2003; Harouna & Perrier 2012; Bhatia *et al.* 2013). In this work, we reconstruct the divergence-free flow field by removing the gradient of harmonic component and solving the following problem:

$$\begin{aligned} \mathscr{P}_{\perp}(\bar{\boldsymbol{u}}_{\mathbf{mri}}):\ & \textit{Given } \bar{\boldsymbol{u}}_{\mathbf{mri}},\ \textit{find } \tilde{\boldsymbol{u}}^{\star} = \bar{\boldsymbol{u}}_{\mathbf{mri}} - \nabla q,\ \textit{such that} \\ & \Delta q = \nabla \cdot \bar{\boldsymbol{u}}_{\mathbf{mri}} \text{ in } \Omega \end{aligned} \tag{3.4}$$

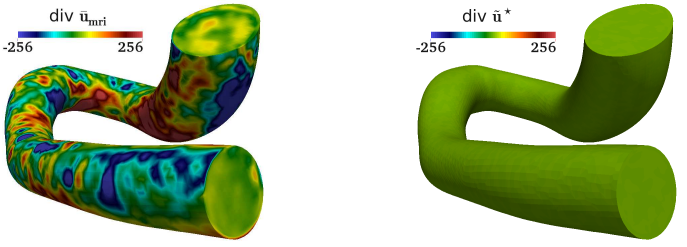

(a) (b)

Figure 3: Divergence of flow field in a phantom of a human aorta acquired with MRI: (a) Raw data, before the application of divergence-free projection operator, $\mathscr{P}_\perp$. (b) Divergence-free flow field, after the application of $\mathscr{P}_\perp$.

$$q = 0 \text{ on } \Gamma_w \quad \text{and} \quad \nabla q \cdot \boldsymbol{n} = 0 \text{ on } \partial\Omega \backslash \Gamma_w \ .$$

The problem $\mathscr{P}_\perp$ presents a projection over a space of divergence-free flow fields. Under certain modifications of the BCs in $\mathscr{P}_\perp$, the HHD can be recovered.

The observations, $\bar{\boldsymbol{u}}_{\mathbf{mri}}$, are assumed to be already modified by the application of the universal outlier detection scheme (as described in section 3.1) prior to its projection in the CFD mesh. The projection ($\boldsymbol{u}^{\circ}_{\mathbf{mri}} \rightarrow \bar{\boldsymbol{u}}_{\mathbf{mri}}$) is performed by linear interpolation. Problem $\mathscr{P}_\perp$ is solved using OpenFOAM's (Weller *et al.* 1998) conjugate gradient solver (PCG) with simplified diagonal-based incomplete Cholesky preconditioner (DIC). Figure 3 illustrates, that the projection into the space of divergence-free vector fields (in the phantom replica of human aorta) recovers the divergence-free property of the flow field to a great extent.

4. Validation of the Methodology

To validate the approach and analyse its performance, we consider the flow of a fluid in a cylindrical geometry, where an analytical solution of a fully developed flow is available. In this work, first an analytical solution is generated for a fine hexahedral mesh of a cylinder. Secondly, a much coarser voxel grid was used to simulate the MRI acquisition pipeline. For each voxel, the MRI simulation was based on the averaged velocity field provided by the fine mesh. Furthermore, some artificial noise was added to the voxel data and, finally, such artificially generated MRI data was put into the preprocessing pipeline described in section 3.

4.1. *Poiseuille Flow*

Consider the fully developed laminar flow of a Newtonian fluid in a cylinder of length L, constant cross-sectional area A, and diameter D ($R = D/2$ the pipe radius). The solution of the Navier-Stokes equations in this case yields

$$\boldsymbol{u}_{\mathbf{ext}}(r) = \frac{\Delta P D^2}{16 \nu \rho L} \left(1 - \frac{r^2}{R^2}\right) \ . \tag{4.1}$$

From (4.1), and calling $\boldsymbol{U}_{\mathbf{avr}}$ the average velocity, it can be derived that $\boldsymbol{u}_{\mathbf{ext}}(r) = 2\boldsymbol{U}_{\mathbf{avr}}\left(1 - r^2/R^2\right)$. Finally, taking $Re = D\boldsymbol{U}_{\mathbf{avr}}/\nu$, the analytical solution can be given in terms of the Reynolds number and kinematic viscosity as,

$$\boldsymbol{u}_{\mathbf{ext}}(r) = \frac{2\nu Re}{D} \left(1 - \frac{r^2}{R^2}\right) \ . \tag{4.2}$$

4.2. *Evaluation of Analytical Solution*

During the MRI acquisition process, the velocities are spatially averaged. To simulate such a framework, the exact solution from equation (4.2) needs to be spatially averaged to the desired MRI voxel size. Since it is not possible to calculate the exact solution for an infinite number of points, its evaluation was performed on each cell center of a fine hexahedral mesh with 3693600 cells. The cylinder radius was $R = 1.2$ cm, and the length was $L = 6$ cm (see figure 4c). As the solution described by Hagen-Poiseuille equation (4.1) is valid for laminar flow, the Re number was chosen to be 2000. Finally, as a reasonable approximation of blood viscosity in human aorta, the kinematic viscosity was chosen to be $\nu = 4.8 \cdot 10^{-6}$ m^2/s. Under these conditions, the maximum flow velocity in the aforementioned cylinder approximately results in $|\boldsymbol{u}|_{max} \approx 0.8$ m/s.

4.3. *Generation of Artificial MRI Data*

Acquired velocities with flow MRI are proportional to the phase-shift in the signal of spins moving along a magnetic gradient field. Since, the phase of a signal is limited to 2π radians, so is also the range of velocities, which can be detected uniquely. The highest velocity, which is likely to be encountered within the region of interest, is hold within a user-defined velocity encoding (VENC). For velocity magnitudes higher than the VENC, the so-called velocity aliasing (or phase wrap-around artifact) occurs, which prevents the unique assignment of the velocities. The quality of flow MRI suffers from velocity noise, which is proportional to velocity encoding and inversely associated to signal-to-noise ratio (SNR) in the related phase difference images (Pelc *et al.* 1991). As described by Pelc *et al.* (1991), the standard deviation of velocity can be approximated as

$$\sigma_u \approx (0.45 * \text{VENC})/\text{SNR} \ . \tag{4.3}$$

Gudbjartsson & Patz (1995) showed that in the existence of noise, the image intensity in phase-contrast MRI is governed by the Rician distribution. For SNR greater than two, the noise distribution is shown to be nearly Gaussian. The analytical solution evaluated in the fine mesh was first averaged into an MRI grid of 2 mm voxel size in each direction as shown in figure 4a. Gaussian white noise was added thereafter on the averaged velocities as shown in figure 4b. VENC was chosen to be 120 cm/s in the longitudinal direction (z), whereas it was 20 cm/s in the remaining directions (x and y). The standard deviation of velocity was chosen such that the noise amplitude corresponds to a SNR of 20. As the cylinder is user-defined, the acquired flow field is already registered with the exact geometry. After the addition of artificial noise, the so simulated MRI data follows the pre-processing pipeline (with exception of the registration stage) as described in section 3, before starting the CFD simulation. In what follows, $\boldsymbol{u}_{\mathbf{snr}}$ will represent the noisy MRI measurements, which are mapped into the computational domain and for which a decomposition is applied to project the field over a divergence-free space as described in sections 3.3 and 3.4. The cylindrical computational domain is illustrated in figure 4c.

4.4. *Optimisation with Exact Solution as Target Flow*

First, we consider one case where the optimisation starts with a noisy flow field and is performed against the exact solution. That is, the target flow field, $\tilde{\boldsymbol{u}}^t$ in the objective function (2.5), corresponds to $\boldsymbol{u}_{\mathbf{ext}}$ given by (4.2). In addition, the initial condition, $(\boldsymbol{u})_0 = \boldsymbol{u}^0$, corresponds to the artificially generated divergence-free flow field, $\boldsymbol{u}_{\mathbf{snr}}$, as described in section 4.3. Thus, algorithm 1 is executed with the input parameters $(\boldsymbol{u}_{\mathbf{snr}}, \boldsymbol{g}_{\mathbf{snr}}, \boldsymbol{u}_{\mathbf{ext}})$, where $\boldsymbol{g}_{\mathbf{snr}} = \boldsymbol{u}_{\mathbf{snr}}$ on Γ_i. In what follows, we will denote $\boldsymbol{u}_{\mathbf{opt}} = \boldsymbol{u}^k_{\mathbf{opt}}$ as the solution returned by the optimisation process after k iterations of algorithm 1. The

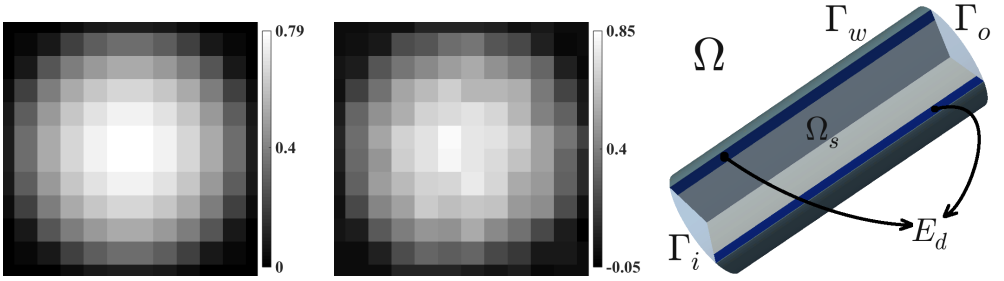

(a) Exact averaged solution (b) Artificial noisy solution (c) Flow Domain

Figure 4: Artificially generated velocity images (2 mm isotropic voxel size) of both the exact solution (a) and the integrated noise with a SNR of 20 (b), before their mapping into the computational flow domain (c).

mesh is set up with 118800 cells including 114840 hexahedras and 3960 prisms. The size of the mesh is suitable to obtain satisfactory results. Flow matching domains, Ω_s, Γ_{si} and Γ_{so} (see figure 4c), cover the lumen including both inlet and outlet boundaries. In what follows, we will give a meaning to the subscript, s, in flow-matching domain, Ω_s. The subscript, s, prescribes the extent of contraction of the whole domain Ω in millimetres (mm), as follows,

$$\Omega_s = \{\, \boldsymbol{x} \in \Omega \mid \|\boldsymbol{x} - \boldsymbol{y}\| \geqslant s\,(\text{mm})\, \forall \boldsymbol{y} \in \Gamma_w \,\} \quad . \tag{4.4}$$

In this set-up, we set $s = 2$. That is, the flow-matching domain, Ω_s, is a contracted domain of, Ω, such that the distance to Γ_w is at least 2 mm. Figure 4c shows the example of Ω_s in the cylinder. Furthermore, the optimisation parameters are $\alpha = 0.15$, $\beta = 10^{-4}$ and $\beta_1 = 10^{-8}$. Figures 5a, 5b and 5c illustrate the norms of the flow matching, $\|\tilde{\boldsymbol{u}}^t - \boldsymbol{u}\|_{\text{fm}}$, the control, $\|\boldsymbol{g}\|_{\text{co}}$, and the surface gradient of the control, $\|\nabla_{\boldsymbol{\tau}}\, \boldsymbol{g}\|_{\text{sg}}$, which are defined as follows:

$$\|\tilde{\boldsymbol{u}}^t - \boldsymbol{u}\|_{\text{fm}} = \left(\frac{100}{\underset{\Omega}{\text{avr}}|\tilde{\boldsymbol{u}}^t|} \right) \sqrt{\frac{1}{V_\Omega} \int_\Omega |\tilde{\boldsymbol{u}}^t - \boldsymbol{u}|^2 \, d\Omega} \quad , \tag{4.5}$$

$$\|\boldsymbol{g}\|_{\text{co}} = \left(\frac{1}{\underset{\Gamma_i}{\text{avr}}|\tilde{\boldsymbol{u}}^t|} \right) \sqrt{\frac{1}{A_{\Gamma_i}} \int_{\Gamma_i} |\boldsymbol{g}|^2 \, d\Gamma} \quad , \tag{4.6}$$

$$\|\nabla_{\boldsymbol{\tau}}\, \boldsymbol{g}\|_{\text{sg}} = \left(\frac{1}{\underset{\Gamma_i}{\text{avr}}|\nabla_{\boldsymbol{\tau}} \tilde{\boldsymbol{u}}^t|} \right) \sqrt{\frac{1}{A_{\Gamma_i}} \int_{\Gamma_i} |\nabla_{\boldsymbol{\tau}} \boldsymbol{g}|^2 \, d\Gamma} \quad , \tag{4.7}$$

where V_Ω is the volume of the entire domain, and A_{Γ_i} is the area at inlet. The norms are normalised against the average magnitude of target velocity or its surface gradient.

As it can be seen in figure 5b, the norm of the control, $\|\boldsymbol{g}\|_{\text{co}}$, rapidly grows at the beginning, forcing the noisy vectors towards their desired position and remaining almost constant after a while. In figure 5c, the sudden decrease in the norm of velocity surface gradient, $\|\nabla_{\boldsymbol{\tau}}\, \boldsymbol{g}\|_{\text{sg}}$, shows the denoising process at inlet. Once a good approximation is reached, the velocities at inlet are only being adjusted slightly during the rest of iterations. This is continued until a sufficient flow matching is achieved in the entire domain as illustrated in figure 5a.

Let us now focus on the results in the domain close to the cylinder wall. To confirm the presented results also with respect to the accuracy in near-wall regions, we calculated

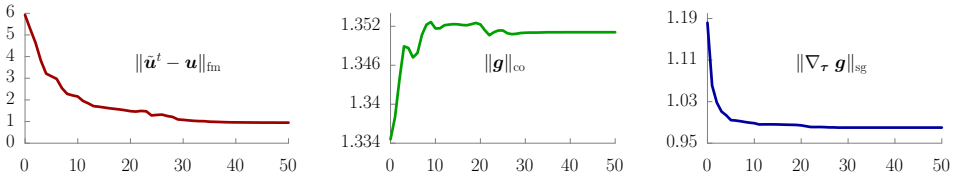

(a) Flow-matching (b) Control (c) Control's surface gradient

Figure 5: The norms from optimisation with parameters $\alpha = 0.15$, $\beta = 10^{-4}$, $\beta_1 = 10^{-8}$. The norms are plotted against the number of iterations in the horizontal axis.

both the root mean square error, $\text{nRMSE}_d = \text{nRMSE}_d(\boldsymbol{u}_{\mathbf{ext}}, \boldsymbol{u}_{\mathbf{opt}})$, and the flow direction error, $\text{FDE}_d = \text{FDE}_d(\boldsymbol{u}_{\mathbf{ext}}, \boldsymbol{u}_{\mathbf{opt}})$, defined by

$$\text{nRMSE}_d(\boldsymbol{u}_t, \boldsymbol{u}_c) = \left(\frac{100}{\underset{E_d}{\text{avr}}|\boldsymbol{u}_t|} \right) \sqrt{\frac{1}{V_d} \int_{E_d} |\boldsymbol{u}_t - \boldsymbol{u}_c|^2 \, dE_d} \quad , \tag{4.8}$$

$$\text{FDE}_d(\boldsymbol{u}_t, \boldsymbol{u}_c) = \sqrt{\frac{1}{V_d} \int_{E_d} \left(1 - \frac{\boldsymbol{u}_t \cdot \boldsymbol{u}_c}{|\boldsymbol{u}_t||\boldsymbol{u}_c|} \right)^2 dE_d} \quad . \tag{4.9}$$

In what follows, the subscript, d, stands for the evaluation of the error within the contracted subdomain $E_d \subset \Omega$ with volume V_d, which is defined as

$$E_d = \{\, \boldsymbol{x} \in \Omega \mid \exists \boldsymbol{y} \in \Gamma_w,\ \|\boldsymbol{x} - \boldsymbol{y}\| < d \text{ (mm)} \,\} \quad . \tag{4.10}$$

That is, we want to evaluate the errors in domain, E_d, at near-wall regions (this domain is not meant to be included in the flow-matching domain Ω_s), where the nearest Euclidean distance of all points in E_d, is at most d mm apart from the wall, Γ_w. Figure 4c features the contracted domain in the cylinder. Note that both errors, (4.8) and (4.9), are evaluated between the exact solution, $\boldsymbol{u}_{\mathbf{ext}}$, and the results obtained from the proposed optimisation strategy, $\boldsymbol{u}_{\mathbf{opt}}$ in the contracted region, E_d. In addition, the error nRMSE_d is normalised against the average velocity magnitude of the observations in E_d.

For $d = 2$, the initial errors $\text{nRMSE}_2(\boldsymbol{u}_{\mathbf{ext}}, \boldsymbol{u}_{\mathbf{snr}})$ and $\text{FDE}_2(\boldsymbol{u}_{\mathbf{ext}}, \boldsymbol{u}_{\mathbf{snr}})$ between the exact solution, $\boldsymbol{u}_{\mathbf{ext}}$, and noisy observations, $\boldsymbol{u}_{\mathbf{snr}}$, were 26.65% and $1.1 \cdot 10^{-2}$, respectively. After optimal control, the root mean square error, as a percentage of average velocity magnitude, were reduced to $\text{nRMSE}_2(\boldsymbol{u}_{\mathbf{ext}}, \boldsymbol{u}_{\mathbf{opt}}) = 3.53\%$ and the flow direction error was $\text{FDE}_2(\boldsymbol{u}_{\mathbf{ext}}, \boldsymbol{u}_{\mathbf{opt}}) = 3.5 \cdot 10^{-5}$.

4.4.1. *Sensitivity Analyses with Respect to Optimisation Parameters*

The differences in the response as a consequence of changes in the optimisation parameters, β and β_1, were examined. First of all, we set $\alpha = 0.15$, which was experimentally found to be an appropriate parameter for this use-case and will then be used in the sensitivity analyses with respect to β and β_1. Secondly, we kept $\beta_1 = 10^{-8}$ fixed and modified β. Figures 6a and 6b show the flow-matching norm, $\|\tilde{\boldsymbol{u}}^t - \boldsymbol{u}\|_{\text{fm}}$, and the control norm, $\|\boldsymbol{g}\|_{\text{co}}$, for different β values. We observed, that for larger values, such as $\beta > 10^{-4}$, there was not enough control and the flow-matching was poor. This is because the objective function was rapidly penalised at early stages of the optimisation, where the optimiser needs larger controls in order to reduce the error. For smaller β values, however, there is no hard penalization and the optimiser can apply larger controls as illustrated in figure 6b. In general, the values 10^{-4} and 10^{-5} delivered satisfactory results and $\beta = 10^{-5}$

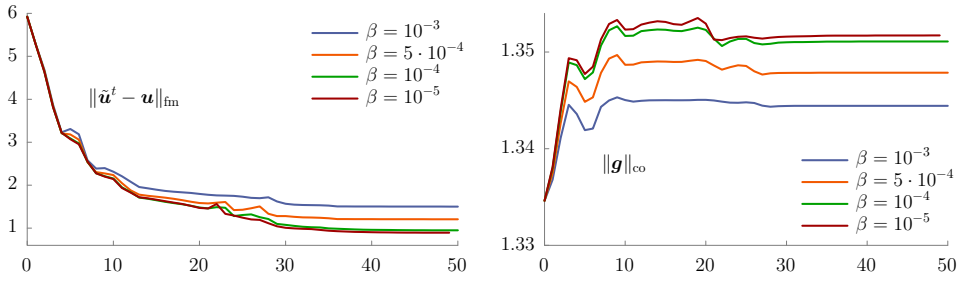

(a) Norms of flow-matching (b) Norms of control

Figure 6: Sensitivities with respect to changes in β, where $\alpha = 0.15$ and $\beta_1 = 10^{-8}$. The norms are plotted against the number of iterations in the horizontal axis.

was observed to be the best choice. Furthermore, we fixed β at 10^{-5} and run the optimiser with β_1 set to 10^{-7}, 10^{-8} and 10^{-9} (smaller values of β_1 rendered unacceptable solutions because of the lack of smoothing effect on noisy measurements), respectively. For different β_1 values, figures 7a and 7c show the plots for the flow-matching norm, $\|\tilde{\boldsymbol{u}}^t - \boldsymbol{u}\|_{\text{fm}}$, and the surface gradient norm, $\|\nabla_{\boldsymbol{\tau}}\, \boldsymbol{g}\|_{\text{sg}}$. Let us first analyse the results between the values 10^{-7} and 10^{-8} for β_1. It can be observed, that the norm of surface gradient is further reduced for $\beta_1 = 10^{-8}$ over the successive iterations and better flow matching is achieved. This can be explained by further investigation of the control norm $\|\boldsymbol{g}\|_{\text{co}}$ in figure 7b. We can observe, that there is no enough control for $\beta_1 = 10^{-7}$. This shows, that even if we are able to remove the noise at inlet (which is explained by the reduction in the value of the surface gradient for $\beta_1 = 10^{-7}$), the controls were small, hence the velocities could not be properly controlled. Secondly, let us consider the results for β_1 values 10^{-8} and 10^{-9}. Figure 7a shows that the flow-matching is achieved with an almost equally good quality. In figure 7b, however, fluctuations along the iterations can be observed in the norm of controls for $\beta_1 = 10^{-9}$. In addition, figure 7c shows that the fluctuations have also an effect on the norm of the surface gradient, which was not as greatly reduced in early iterations, as it was the case for $\beta_1 = 10^{-8}$. Finally, our interpretations are also confirmed quantitatively at near-wall regions. Table 1 summarises the results from the sensitivity analysis comparing the root mean square errors, nRMSE_2, and the flow direction errors, FDE_2 for varying optimisation parameters. Our conclusion is that setting $\beta_1 = 10^{-8}$ delivers sufficiently accurate results and will be used in hereafter.

4.5. *Optimisation with Noisy Solution as Target Flow*

So far, we were able to validate the proposed approach using an analytical solution. Actually, an exact solution is not available or cannot be provided by measurements or experiments. Here, the performance of the optimisation framework was evaluated considering the artificially generated noisy measurements as the target flow. That is, we set $\tilde{\boldsymbol{u}}^t = \boldsymbol{u}_{\mathbf{snr}}$ in the objective function (2.5). In order to avoid lack of control, the initial flow field was low-pass filtered with a cutoff frequency of 0.5. The resulting flow field is represented by $\boldsymbol{u}_{\mathbf{lpf}}$ in Ω and the algorithm 1 was executed with the input parameters $(\boldsymbol{u}_{\mathbf{lpf}}, \boldsymbol{g}_{\mathbf{lpf}}, \boldsymbol{u}_{\mathbf{snr}})$, where $\boldsymbol{g}_{\mathbf{lpf}} = \boldsymbol{u}_{\mathbf{lpf}}$ on Γ_i. Motivated by the findings of the previous section, parameters β and β_1 were set to 10^{-5} and 10^{-8}, respectively. As before, the flow matching was performed in Ω_s with $s = 2$. Parameter α was adjusted to 0.5 for this

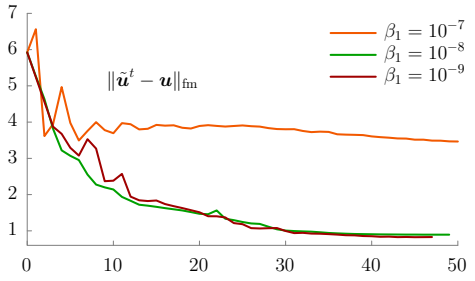

(a) Norms of flow-matching

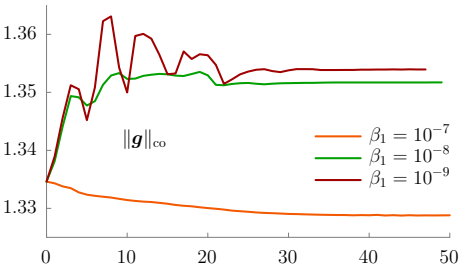

(b) Norms of control

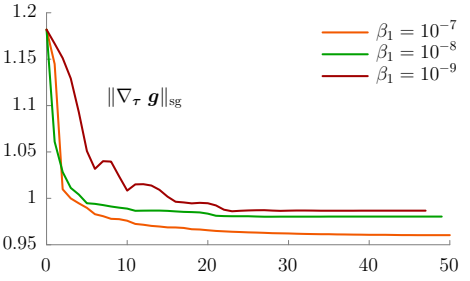

(c) Norms of control surface gradient

Figure 7: Sensitivities with respect to changes in β_1, where $\alpha = 0.15$ and $\beta = 10^{-5}$. The norms are plotted against the number of iterations in the horizontal axis.

(β, β_1)	$(10^{-3}, 10^{-8})$	$(10^{-4}, 10^{-8})$	$(10^{-5}, 10^{-8})$	$(10^{-5}, 10^{-9})$	$(10^{-5}, 10^{-7})$
$\mathbf{nRMSE}_2(\boldsymbol{u}_{\mathbf{ext}}, \boldsymbol{u}_{\mathbf{opt}})$	4.53 %	3.53 %	3.41 %	3.68 %	8.40 %
$\mathbf{FDE}_2(\boldsymbol{u}_{\mathbf{ext}}, \boldsymbol{u}_{\mathbf{opt}})$	$7.0 \cdot 10^{-5}$	$3.5 \cdot 10^{-5}$	$2.8 \cdot 10^{-5}$	$1.4 \cdot 10^{-4}$	$4.8 \cdot 10^{-5}$

Table 1: Dimensionless root mean square ($\text{nRMSE}_2(\boldsymbol{u}_{\mathbf{ext}}, \boldsymbol{u}_{\mathbf{opt}})$) and flow direction ($\text{FDE}_2(\boldsymbol{u}_{\mathbf{ext}}, \boldsymbol{u}_{\mathbf{opt}})$) errors measured within the near-wall (2 mm) domain (E_2).

set-up. Under these conditions, the quantitative results yielded 4.85% and $5.8 \cdot 10^{-5}$ for nRMSE_2 and FDE_2, respectively.

4.5.1. *Sensitivity Analyses with Respect to Flow-Matching Domain*

As described in section 4.3, the addition of artificial noise follows the same procedure at each location in the flow domain and does not depend on the velocity magnitudes. Hence, the near-wall regions with very low velocities contain almost no relevant signal, but mostly noise. Moreover, near-wall regions also contain further errors due to partial volume effects. Hence, such locations should rather be avoided in the flow-matching domain, Ω_s. Therefore, a further contraction in the subdomain was considered in addition. To account for it, we performed a sensitivity analysis with respect to changes in the flow-matching domain Ω_s, using the same parameters as specified above. The simulations were performed with varying s ranging from 1.5 to 4.

The norms of the control are shown in figure 8a for different values of s. It can be observed, that larger controls result for $s = 2.5$. The magnitude of the control $\boldsymbol{g}$ decreases if Ω_s is further contracted or extended. This can be also confirmed by nRMSE_d in figure

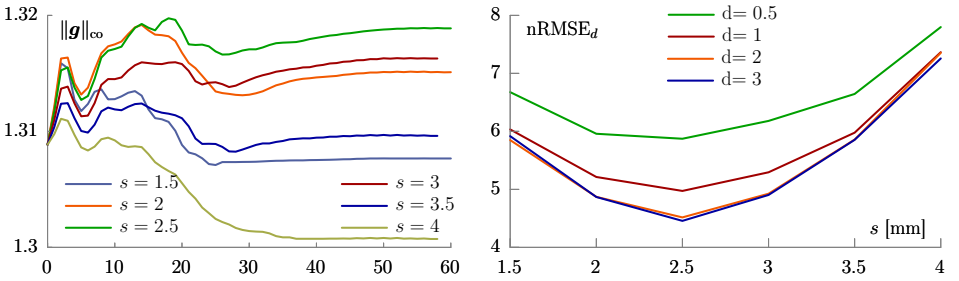

(a) Sensitivities against changes in s (b) Errors plotted against s for different d

Figure 8: Illustration of (a): norm of controls with respect to changes in flow-matching domain, Ω_s, and (b): root-mean-square errors at near-wall domain, E_d. The norms are plotted against the number of iterations in the horizontal axis.

8b, where the x-axes represents s. The errors at near-wall regions are further decreased for $s = 2.5$. In addition, figure 8b illustrates the error measurements (y-axes) for different values of d represented in different colours. It can be observed that in all cases, the optimisation framework delivers accurate results at locations of the domain close to the lateral boundary (the wall). This is especially interesting for the evaluation of wall shear stresses, one of the most important parameters for diagnostic purposes in the cardiovascular field. Table 2 summarises the results in the near-wall domains E_d defined for different distances from the wall (with d values ranging from 3 mm to 0.5 mm) for varying flow-matching domains Ω_s with varying s ranging from 1.5 to 4. E.g., for a flow-matching domain $\Omega_{2.5}$, which is 2.5 mm apart from the wall Γ_w, the root-mean-square error nRMSE$_2$, which is evaluated within 2 mm distance of the wall Γ_w, was 4.52%, and FDE$_{0.5}$ was $5.0 \cdot 10^{-5}$. This improves the accuracy in comparison to the results from previous section, where the flow-matching domain was chosen to be Ω_2. For $s \geqslant 3$, the accuracy also starts dropping. This is a remarkable finding for the choice of Ω_s. In general, the flow-matching domain should be constructed such that it contains almost all available information about the flow field in the luminal area (reaching from inlet to outlet), whereas it should avoid using the information at near-wall locations. We have shown that keeping the flow-matching domain 2.5 (mm) away from the vessel wall is a very good choice for this case.

4.5.2. *Comparison against classical CFD*

Finally, the ability of boundary control approach to the measured flow field in the entire domain was compared against the results delivered from the *classical* CFD strategy. The latter is based on a single forward simulation, with Dirichlet boundary conditions, applied (as usual) at the inlet boundary. Then, the classical CFD implies solving the problem $\mathscr{P}_{\text{sta}}$, as stated by the variational equations (2.18)-(2.19)-(2.20). Thus, using the initial guess $\boldsymbol{u}_{\mathbf{snr}}$ and the BC $\boldsymbol{u} = \boldsymbol{u}_{\mathbf{snr}}$ on Γ_i, the linearised problem $\mathscr{P}^{\text{lin}}_{\text{sta}}(\boldsymbol{u}_{\mathbf{snr}}, \boldsymbol{g}_{\mathbf{snr}})$ was solved with $\boldsymbol{g}_{\mathbf{snr}} = \boldsymbol{u}_{\mathbf{snr}}$ on Γ_i, iteratively until convergence is achieved. In what follows, the solution obtained from a classical CFD approach will be denoted as $\boldsymbol{u}_{\mathbf{cfd}}$. Motivated by the conclusion in section 4.5.1, the optimisation algorithm was employed to deliver the optimised solution $\boldsymbol{u}_{\mathbf{opt}}$ for parameters $\alpha = 0.5$, $\beta = 10^{-5}$, $\beta_1 = 10^{-8}$ and $s = 2.5$. Furthermore, the optimisation is performed against the noisy solution as target flow and initialised with the low-pass filtered flow field, as described in section 4.5. We want to

s	1.5	2	2.5	3	3.5	4
$\mathbf{nRMSE}_3$	5.92 %	4.86 %	4.46 %	4.90 %	5.85 %	7.26 %
$\mathbf{FDE}_3$	$6.1 \cdot 10^{-5}$	$4.8 \cdot 10^{-5}$	$4.2 \cdot 10^{-5}$	$4.4 \cdot 10^{-5}$	$4.7 \cdot 10^{-5}$	$5.0 \cdot 10^{-5}$
$\mathbf{nRMSE}_2$	5.85 %	4.85 %	4.52 %	4.92 %	5.86 %	7.35 %
$\mathbf{FDE}_2$	$7.5 \cdot 10^{-5}$	$5.8 \cdot 10^{-5}$	$5.0 \cdot 10^{-5}$	$5.3 \cdot 10^{-5}$	$5.7 \cdot 10^{-5}$	$6.0 \cdot 10^{-5}$
$\mathbf{nRMSE}_1$	6.03 %	5.18 %	4.97 %	5.29 %	5.98 %	7.36 %
$\mathbf{FDE}_1$	$1.0 \cdot 10^{-4}$	$7.9 \cdot 10^{-5}$	$6.9 \cdot 10^{-5}$	$7.3 \cdot 10^{-5}$	$7.7 \cdot 10^{-5}$	$8.2 \cdot 10^{-5}$
$\mathbf{nRMSE}_{0.5}$	6.68 %	5.93 %	5.88 %	6.18 %	6.64 %	7.80 %
$\mathbf{FDE}_{0.5}$	$1.3 \cdot 10^{-4}$	$1.0 \cdot 10^{-4}$	$8.7 \cdot 10^{-5}$	$9.2 \cdot 10^{-5}$	$9.8 \cdot 10^{-5}$	$1.0 \cdot 10^{-4}$

Table 2: Dimensionless root mean square, $\mathrm{nRMSE}_d(\boldsymbol{u}_{\mathbf{ext}}, \boldsymbol{u}_{\mathbf{opt}})$, and flow direction, $\mathrm{FDE}_d(\boldsymbol{u}_{\mathbf{ext}}, \boldsymbol{u}_{\mathbf{opt}})$, errors measured within the near-wall (d (mm)) domain, E_d, for varying flow-matching domains, Ω_s (s (mm) apart from the wall).

emphasise that, during the optimisation procedure, there is no knowledge available about the exact solution at all.

Flow patterns were first inspected visually to obtain a qualitative interpretation. Figure 9 shows the flow patterns in the domain, obtained from the artificially generated noisy measurements, $\boldsymbol{u}_{\mathbf{snr}}$, the computations via the traditional CFD method, $\boldsymbol{u}_{\mathbf{cfd}}$, the computations from the proposed optimisation framework, $\boldsymbol{u}_{\mathbf{opt}}$, and finally the exact solution, $\boldsymbol{u}_{\mathbf{ext}}$. It can be appreciated that the optimised flow is the one that better resembles the exact solution. Especially, it features excellent qualitative agreement with the exact solution at the inlet boundary and at locations near to the inlet, where the traditional CFD approach suffers from inaccuracy, caused by the noisy boundary condition.

To confirm the previous qualitative assessment, the simulation results from both the classical CFD and the control approaches were quantitatively compared against the exact solution. First, we evaluated nRMSE_d and FDE_d in the near-wall domain E_d for the values $d = 2$, $d = 1$ and $d = 0.5$. Table 3 shows that the velocity field was reconstructed by the optimisation algorithm much more accurately at the wall boundary, in comparison to the classical CFD approach. Noisy observations, $\boldsymbol{u}_{\mathbf{snr}}$, deliver almost no relevant signal near the boundaries, which can be observed by the huge and increasing errors for decreasing d values. In contrast, however, nRMSE_d is more rapidly decreased when applying the optimisation algorithm to obtain $\boldsymbol{u}_{\mathbf{opt}}$, as we get closer to wall boundary. This shows the feasibility of the optimisation approach, especially for its accuracy at the boundaries. Furthermore, the flow direction errors are decreased to a much greater extent for the optimised flow in comparison to the classical CFD method. This also shows clearly that the noise at the inlet boundary was removed to a great extent by the application of the control. In addition, it can be seen that FDE_d is not further decreased as we get close to the walls. This is expected, since the optimisation procedure itself is a trade-off between decreasing the flow-matching errors in terms of magnitudes and the flow direction errors based on the surface gradient. Both terms are included in the objective function and are affected by the choice of parameters.

Finally, the maximum and average wall shear stresses were calculated from the numerical results based on the classical CFD and from the optimisation procedure. These quantities were then compared against the wall shear stresses computed with the analytical solution. Figure 10 shows the box plots to characterise the discrepancies between

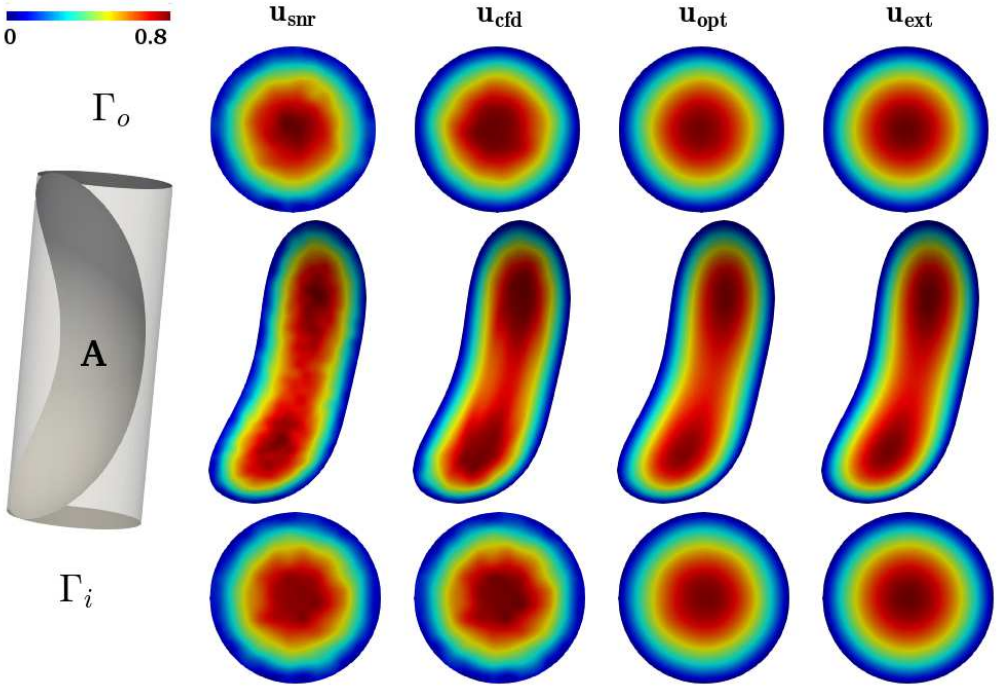

Figure 9: Flow patterns for fields $\boldsymbol{u}_{\mathbf{snr}}$, $\boldsymbol{u}_{\mathbf{cfd}}$, $\boldsymbol{u}_{\mathbf{opt}}$ and $\boldsymbol{u}_{\mathbf{ext}}$ illustrated at inlet (Γ_i), outlet (Γ_o) and at a curved surface (A) immersed in the lumen. The colours representing the velocity magnitudes are scaled to the range of 0 and 0.8, whereas the corresponding maximum velocities were $|\boldsymbol{u}_{\mathbf{snr}}|_{max} \approx 0.853$, $|\boldsymbol{u}_{\mathbf{cfd}}|_{max} \approx 0.777$, $|\boldsymbol{u}_{\mathbf{opt}}|_{max} \approx 0.784$ and $|\boldsymbol{u}_{\mathbf{ext}}|_{max} \approx 0.8$.

$\boldsymbol{x} = \boldsymbol{u}_{\mathbf{ext}}$	$\mathbf{nRMSE_d}(\boldsymbol{x}, \boldsymbol{y})$			$\mathbf{FDE_d}(\boldsymbol{x}, \boldsymbol{y})$		
	$\boldsymbol{y} = \boldsymbol{u}_{\mathbf{snr}}$	$\boldsymbol{y} = \boldsymbol{u}_{\mathbf{cfd}}$	$\boldsymbol{y} = \boldsymbol{u}_{\mathbf{opt}}$	$\boldsymbol{y} = \boldsymbol{u}_{\mathbf{snr}}$	$\boldsymbol{y} = \boldsymbol{u}_{\mathbf{cfd}}$	$\boldsymbol{y} = \boldsymbol{u}_{\mathbf{opt}}$
$d = 2$	26.65 %	8.36 %	4.52 %	$1.1 \cdot 10^{-2}$	$1.2 \cdot 10^{-3}$	$5.0 \cdot 10^{-5}$
$d = 1$	61.30 %	11.79 %	4.97 %	$1.6 \cdot 10^{-2}$	$1.7 \cdot 10^{-3}$	$6.9 \cdot 10^{-5}$
$d = 0.5$	139.82 %	17.93 %	5.88 %	$2.1 \cdot 10^{-2}$	$2.1 \cdot 10^{-3}$	$8.7 \cdot 10^{-5}$

Table 3: Dimensionless root mean square ($\mathrm{nRMSE}_d(\boldsymbol{u}_{\mathbf{ext}}, \boldsymbol{y})$) and flow direction ($\mathrm{FDE}_d(\boldsymbol{u}_{\mathbf{ext}}, \boldsymbol{y})$) errors for $\boldsymbol{y} = \{\, \boldsymbol{u}_{\mathbf{snr}}, \boldsymbol{u}_{\mathbf{cfd}}, \boldsymbol{u}_{\mathbf{opt}} \,\}$, measured within the near-wall (d mm) domain (E_d). Optimisation is performed using measurements in the flow-matching volume (Ω_s), which is ($s = 2.5$ mm) apart from the wall boundary.

the WSS field obtained from the exact solution, $\boldsymbol{u}_{\mathbf{ext}}$, and the WSS fields obtained from both the computations with classical CFD, $\boldsymbol{u}_{\mathbf{cfd}}$, and the optimised solution, $\boldsymbol{u}_{\mathbf{opt}}$.

5. Data Assimilation in a Realistic Geometry

The proposed approach was tested for the flow-matching control problem in a more realistic geometry obtained from a glass replica of a human aorta. The geometry consists of aortic root, ascending aorta, aortic arch without branches and descending aorta as

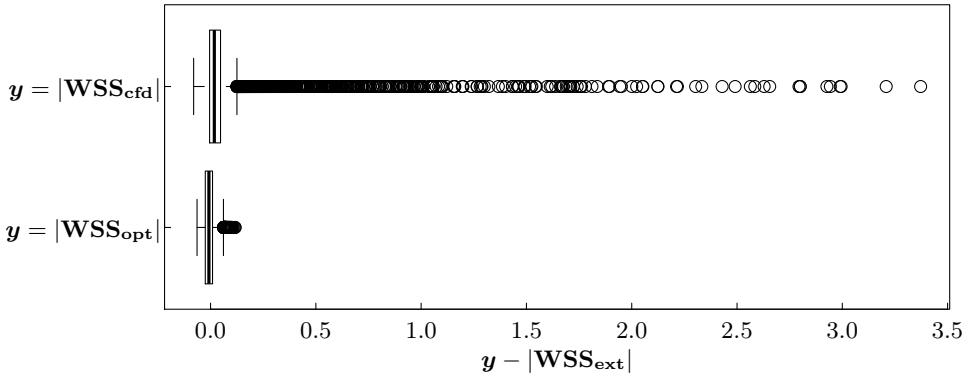

Figure 10: Box plot illustrating the differences ($|\mathbf{WSS_{cfd}}| - |\mathbf{WSS_{ext}}|$) and ($|\mathbf{WSS_{opt}}| - |\mathbf{WSS_{ext}}|$) in the horizontal axis, where the labels $\mathbf{WSS_{cfd}}$, $\mathbf{WSS_{opt}}$ and $\mathbf{WSS_{ext}}$ represent the wall shear stresses corresponding to the fields $\boldsymbol{u}_{\mathbf{cfd}}$, $\boldsymbol{u}_{\mathbf{opt}}$ and $\boldsymbol{u}_{\mathbf{ext}}$, respectively.

illustrated in figure 1a. Optimisation results were first compared with measured data both qualitatively and quantitatively. In addition, the results were compared against the results when using classical CFD method prescribing Dirichlet boundary conditions. Furthermore, a sensitivity analysis with respect to changes in the initial guess flow field were analysed and discussed. Finally, the proposed approach was tested under flow conditions with increasing *Re* numbers ranging approximately from 1200 up to 7100.

5.1. *Experimental Setup*

The in-vitro experiment was prepared in a scanner and control room including a 3T MRI scanner from Philips. The glass replica, covered by a 6-element cardiac coil, was placed in the scanner and connected to a centrifugal pump (in the control room) with a maximum pressure of 3.9 bar. The connection was made with a PVC tubing of total length 20 m with an inner diameter of 19 mm. The inlet and outlet of the pipe were connected to a reservoir in the control room creating an open circuit. A ball bearing valve was placed 1.5 m downstream the tube and was used to control the flow rate. Figure 11 illustrates the experimental setup.

The reservoir was filled with a mixture of 24 liter H_2O, 40 gr carboxymethyl cellulose carboxymethyl (CMC) and 10 gr sulfate. The aim of CMC medium was to increase the viscosity of the fluid to an approximately similar level of blood viscosity. On the other side, sulfate acted as a contrast agent to increase the signal magnitude. For a temperature of 27° C, the mixture featured a viscosity of 3.5 cP.

Five different image acquisitions were performed to obtain data with increasing *Re* numbers. The maximum velocities in the obtained data were $1.06, 1.71, 2.26, 3.47$ and 4.88 m/s and the corresponding *Re* numbers were $1223, 1860, 2105, 4636$ and 7171, respectively. Thus, the flow rates were controlled such that the obtained data first contained laminar flow, then included transitional regions, and finally, consisted of turbulent flow. We highlight that the flow model does not account for turbulence, and therefore we acknowledge the model deficiency for high *Re* numbers. Even so, we report the results to demonstrate the capabilities of the methodology under extreme conditions. Consideration of turbulence models is matter of current research.

A 3-D spoiled Gradient-Echo sequence with flow encoding gradients was used for the flow-MRI acquisitions. The eddy-current induced background phase was compensated

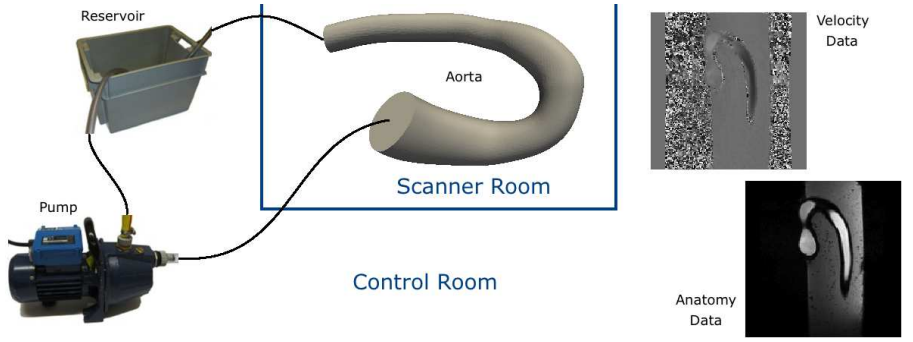

Figure 11: Experimental setup for the glass replica of human aorta.

by application of linear phase correction. The acquisition parameters were chosen as flip angle: 10^o, time of repetition and echo (TR/TE): 2.6/4.87 ms, field of view (FOV): $[244 \times 244 \times 62]$ mm^3 and voxel size: $[1.4 \times 1.4 \times 1.5]$ mm^3. Furthermore, considering the increasing Re numbers of the measured data, the corresponding VENCs were chosen as $120, 200, 260, 380$ and 520 cm/s, respectively.

5.2. *Data Preprocessing*

For the generation of the computational mesh, the aortic replica was first segmented (see figure 12a) from the anatomical data and then smoothed (see figure 12b). Thereafter, the available exact geometry (see figure 12d), with the region of interest which defines the inlet/outlet boundaries highlighted, was registered with the smoothed geometry as shown in figure 12c. Finally, a hexahedral mesh with 122079 cells was created using the exact geometry cut by the region of interest. Figures 12e–12f illustrate the computational mesh.

Having the computational mesh generated, the measured flow data followed into the preprocessing pipeline as described in section 3. In what follows, $\boldsymbol{u}_{\mathbf{snr}}^{Re}$ with $Re = \{\, 1223, 1860, 2105, 4636, 7171 \,\}$ will represent the flow fields derived after the application of divergence-free space projection, that is after solving the problem $\mathscr{P}_\perp$ described by the equation (3.4).

5.3. *Simulation Results*

We will first present the numerical results for $Re = 1223$ based on the flow data denoted by, $\boldsymbol{u}_{\mathbf{snr}}^{Re}$, mapped on the computational mesh domain and projected into a divergence-free space. In what follows, $\boldsymbol{u}_{\mathbf{snr}}^{Re}$ with $Re = 1223$ will be simply denoted as $\boldsymbol{u}_{\mathbf{snr}}$. The target flow in the objective function (2.5) is set as $\tilde{\boldsymbol{u}}^t = \boldsymbol{u}_{\mathbf{snr}}$. A low-pass filtered flow field of this target flow with a cut-off frequency of 4 was used as the initial guess, which will be denoted as $(\boldsymbol{u})_0 = \boldsymbol{u}_{\mathbf{lpf}}^{4.0}$. The frequency was chosen such that the flow field being low-pass filtered is not over-smoothed and remains close to the actual target field. The maximum magnitude of low-pass filtered flow data was 0.98 m/s, whereas for the target flow it was 1.06 m/s. Flow matching was performed in Ω_s with $s = 2.5$ and the optimisation parameters were chosen as $\beta = 10^{-5}$, $\beta_1 = 10^{-6}$ and $\alpha = 0.25$. That is, algorithm 1 is executed in the domain as represented in figure 1a with the input parameters $(\boldsymbol{u}_{\mathbf{lpf}}^{4.0}, \boldsymbol{g}_{\mathbf{lpf}}^{4.0}, \boldsymbol{u}_{\mathbf{snr}})$, where $\boldsymbol{g}_{\mathbf{lpf}}^{4.0} = \boldsymbol{u}_{\mathbf{lpf}}^{4.0}$ on Γ_i.

The flow patterns predicted by the optimisation algorithm and by the classical CFD method were first qualitatively compared against the measured data by visual inspection. Figure 13 shows the streamlines corresponding to the different velocity fields. Figure 14

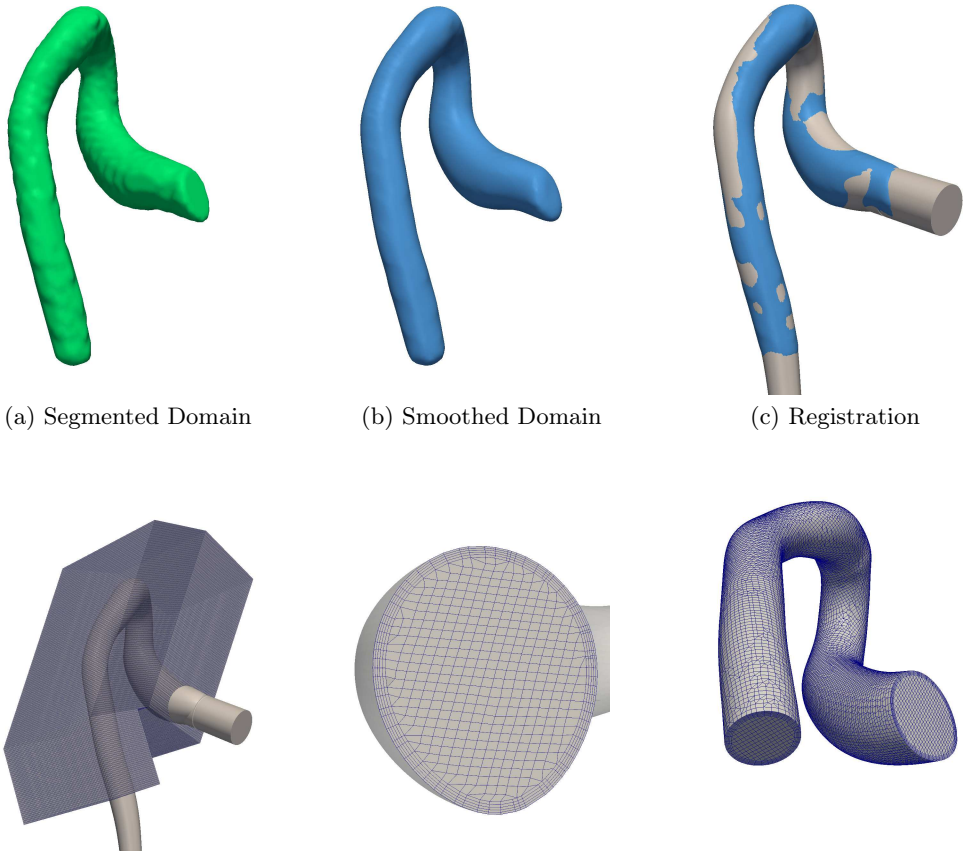

(a) Segmented Domain (b) Smoothed Domain (c) Registration

(d) Exact Geometry (e) Mesh at Inlet (f) Mesh in Domain

Figure 12: Mesh generation from exact geometry (d) including the segmentation (a) of domain from anatomical data, smoothing (b) and registration (c) of exact geometry with the smoothed geometry. A region of interest (d) defines the computational domain for which a hexahedral mesh with 122079 cells is created (e), (f).

illustrates the magnitude of the velocity field in a cross-sectional slice covering part of the ascending and descending aorta. Furthermore, figure 15 highlights the wraps of the velocity profile for a set of transversal slices. It can be observed that the measured velocity field, $\boldsymbol{u}_{\mathbf{snr}}$, and the optimised solution, $\boldsymbol{u}_{\mathbf{opt}}$, are reasonably similar, whereas the flow field predicted by the classical CFD method is relatively far from the measured data.

The results were also analysed quantitatively and compared against the measured data. The flow matching norm between the observations and optimised flow, $\|\tilde{\boldsymbol{u}}^t - \boldsymbol{u}_{\mathbf{opt}}\|_{\mathrm{fm}}$, resulted in 37% of the average velocity magnitude of observations, whereas the norm between the observations and the computations from traditional CFD method, $\|\tilde{\boldsymbol{u}}^t - \boldsymbol{u}_{\mathbf{cfd}}\|_{\mathrm{fm}}$, was 50%. This supports the fact, that the optimisation delivers a better solution when compared with the classical CFD approach. Furthermore, the root-mean-square errors, $\mathrm{nRMSE}_d(\boldsymbol{u}_{\mathbf{snr}}, \boldsymbol{u}_{\mathbf{opt}})$, were evaluated at near-wall regions. For $d = 2, 1, 0.5$, the errors were 49, 65 and 82 % of average flow magnitude of observed data, respectively. As expected in this case, the computed flow diverges even more from the observed data, as getting closer to the wall. This is due to the fact that the phantom material itself delivers almost no relevant signal at and near the boundary, but mainly noise. For the classical

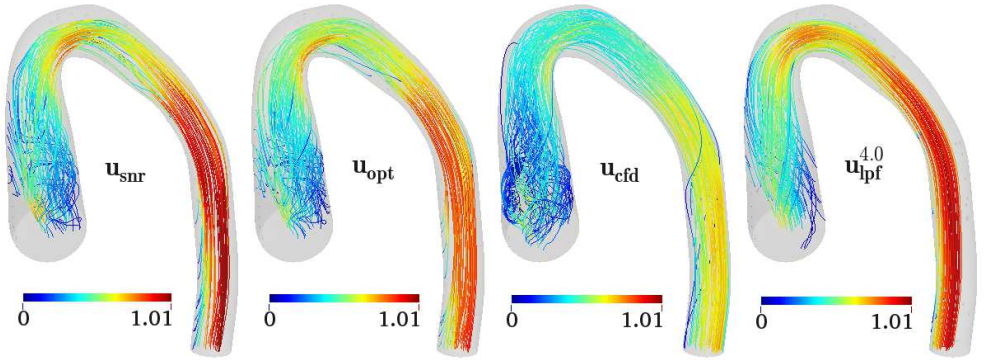

Figure 13: Streamlines for the different velocity fields.

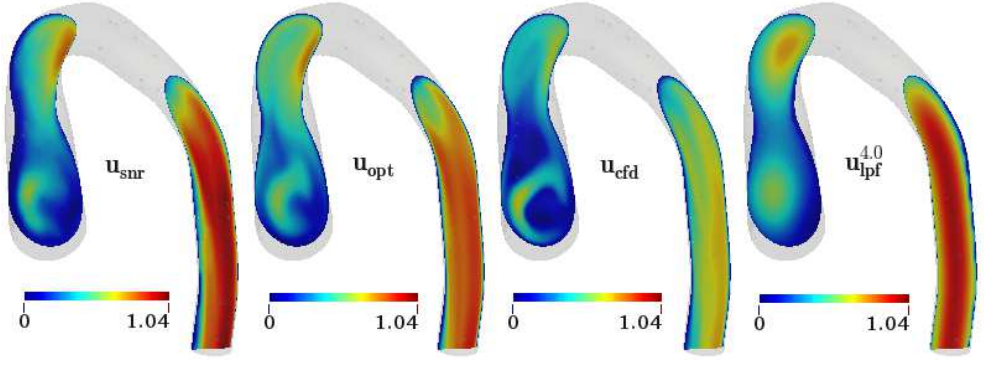

Figure 14: Velocity magnitude in a cross-sectional slice for the different velocity fields.

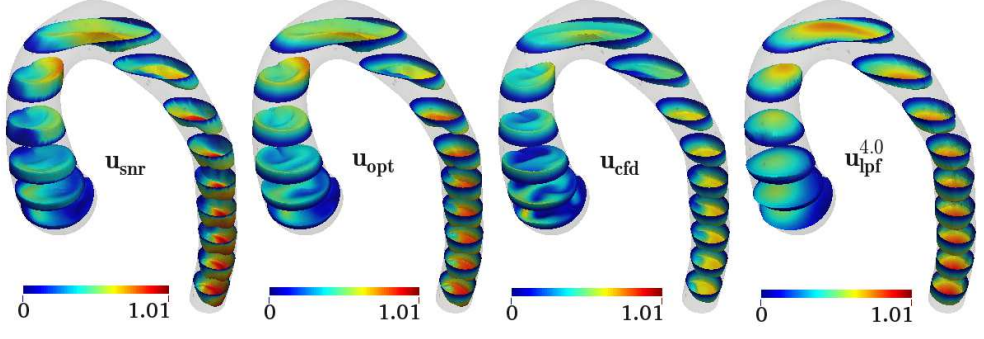

Figure 15: Wraps of the velocity fields at a set of cross-sectional slices.

CFD method, $\text{nRMSE}_d(\boldsymbol{u}_{\mathbf{snr}}, \boldsymbol{u}_{\mathbf{cfd}})$ was 52, 68 and 89 % for $d = 2, 1, 0.5$, respectively. In addition, we evaluated the errors between $\boldsymbol{u}_{\mathbf{cfd}}$ and $\boldsymbol{u}_{\mathbf{opt}}$ to quantify the differences of the flow fields predicted by the classical CFD method and the optimisation strategy. For $d = 2, 1, 0.5$, the errors $\text{nRMSE}_d(\boldsymbol{u}_{\mathbf{cfd}}, \boldsymbol{u}_{\mathbf{opt}})$ were 41, 46 and 49 %, respectively. This shows, that the differences in the predictions grow as getting closer to the wall. The normalised difference, $\|\mathbf{WSS}_{\mathbf{cfd}} - \mathbf{WSS}_{\mathbf{opt}}\|$ (see equations (5.1) and (5.2)), between the WSS fields corresponding to the velocity fields $\boldsymbol{u}_{\mathbf{cfd}}$ and $\boldsymbol{u}_{\mathbf{opt}}$ was 43.72%. Furthermore,

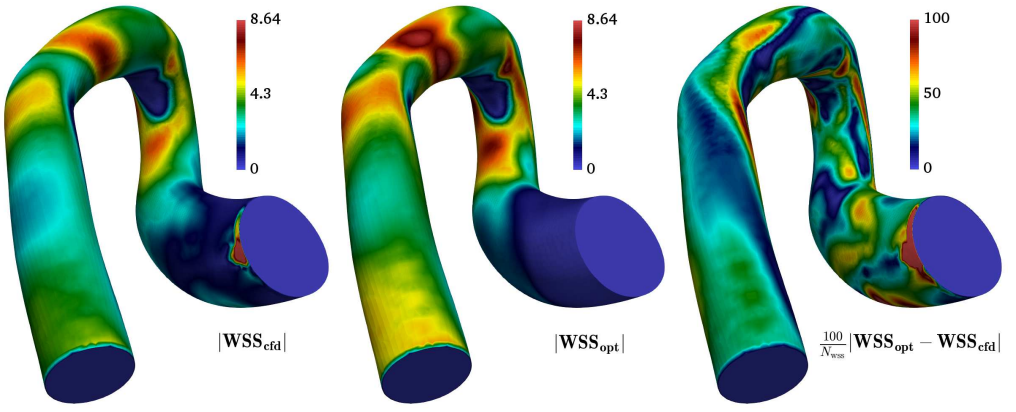

(a) (b) (c)

Figure 16: (a), (b): Magnitude fields of wall shear stresses, $|\mathbf{WSS}_{\mathbf{cfd}}|$ and $|\mathbf{WSS}_{\mathbf{opt}}|$, corresponding to the velocity fields $\boldsymbol{u}_{\mathbf{cfd}}$ and $\boldsymbol{u}_{\mathbf{opt}}$, (c): Normalised difference field, $\frac{100}{N_{\mathrm{wss}}}|\mathbf{WSS}_{\mathbf{opt}} - \mathbf{WSS}_{\mathbf{cfd}}|$ on Γ_w, where N_{wss} is as described in equation (5.1)

figures 16a and 16b illustrate the magnitudes of the WSS fields, $\mathbf{WSS}_{\mathbf{cfd}}$ and $\mathbf{WSS}_{\mathbf{opt}}$, and figure 16c shows their normalised difference field. In addition, figures 17a and 17b illustrate the pressure fields of the predictions from the classical CFD method and from the optimisation strategy, respectively, whereas figure 17c shows their normalised difference field.

$$N_{\mathrm{wss}} = \frac{1}{A_{\Gamma_w}} \int_{\Gamma_w} \frac{|\mathbf{WSS}_{\mathbf{opt}} + \mathbf{WSS}_{\mathbf{cfd}}|}{2}\, d\Gamma \quad , \tag{5.1}$$

$$\|\mathbf{WSS}_{\mathbf{opt}} - \mathbf{WSS}_{\mathbf{cfd}}\| = \frac{100}{N_{\mathrm{wss}}} \sqrt{\frac{1}{A_{\Gamma_w}} \int_{\Gamma_w} |\mathbf{WSS}_{\mathbf{opt}} - \mathbf{WSS}_{\mathbf{cfd}}|^2\, d\Gamma} \quad . \tag{5.2}$$

5.4. *Sensitivity with Respect to Initial Guess*

To analyse the performance and sensitivity of the optimisation strategy with respect to changes in the initial guess, different flow fields were generated from the observations to be applied as initial guess flow. The observations were low-pass filtered with varying cut-off frequency 3.5 and 4.5, denoted as $\boldsymbol{u}_{\mathbf{lpf}}^{3.5}$ and $\boldsymbol{u}_{\mathbf{lpf}}^{4.5}$, respectively. The maximum velocity magnitude was 1.16 m/s for the flow field $\boldsymbol{u}_{\mathbf{lpf}}^{3.5}$, whereas it was 0.84 m/s for $\boldsymbol{u}_{\mathbf{lpf}}^{4.5}$. In addition, a zero flow field, $\boldsymbol{u}_0$, was prepared as initial guess, that is $\boldsymbol{u}_0 = \mathbf{0}$ in Ω. Under the same conditions as in section 5.3, algorithm 1 was executed with input parameters $(\boldsymbol{u}_{\mathbf{lpf}}^{3.5}, \boldsymbol{g}_{\mathbf{lpf}}^{3.5}, \boldsymbol{u}_{\mathbf{snr}})$, $(\boldsymbol{u}_{\mathbf{lpf}}^{4.5}, \boldsymbol{g}_{\mathbf{lpf}}^{4.5}, \boldsymbol{u}_{\mathbf{snr}})$, $(\boldsymbol{u}_{\mathbf{snr}}, \boldsymbol{g}_{\mathbf{snr}}, \boldsymbol{u}_{\mathbf{snr}})$ and $(\boldsymbol{u}_0, \boldsymbol{g}_{\mathbf{snr}}, \boldsymbol{u}_{\mathbf{snr}})$, where $\boldsymbol{g}_{\mathbf{lpf}}^{3.5} = \boldsymbol{u}_{\mathbf{lpf}}^{3.5}$, $\boldsymbol{g}_{\mathbf{lpf}}^{4.5} = \boldsymbol{u}_{\mathbf{lpf}}^{4.5}$ and $\boldsymbol{g}_{\mathbf{snr}} = \boldsymbol{u}_{\mathbf{snr}}$ on Γ_i, correspondingly.

Visual inspection revealed no remarkable differences in the final optimised velocity fields. Table 4 shows the flow-matching norms, the averaged WSS and the number of iterations for the optimisation starting with initial conditions, $\boldsymbol{u}_{\mathbf{snr}}$, $\boldsymbol{u}_0$, $\boldsymbol{u}_{\mathbf{lpf}}^{3.5}$, $\boldsymbol{u}_{\mathbf{lpf}}^{4.0}$ and $\boldsymbol{u}_{\mathbf{lpf}}^{4.5}$, respectively. Both the qualitative and quantitative results indicate that there was no significant changes in the solution with respect to changes in the initial guess provided

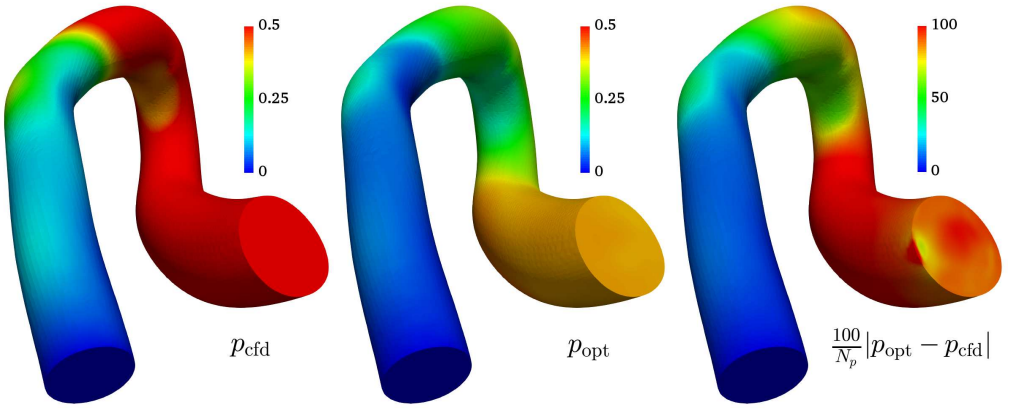

(a) (b) (c)

Figure 17: Pressure fields corresponding to predictions from classical CFD, p_{cfd}, from optimisation strategy, p_{opt}, and their normalised difference field, $\dfrac{100}{N_p}\,|p_{\text{opt}} - p_{\text{cfd}}|$ on $\partial\Omega$, where $N_p = \dfrac{1}{V_\Omega}\displaystyle\int_\Omega \frac{|p_{\text{opt}} + p_{\text{cfd}}|}{2}\, d\Omega$.

Init. Guess	$(\boldsymbol{u})_0 = \boldsymbol{u}_{\mathbf{snr}}$	$(\boldsymbol{u})_0 = \boldsymbol{u}_0$	$(\boldsymbol{u})_0 = \boldsymbol{u}^{3.5}_{\mathbf{lpf}}$	$(\boldsymbol{u})_0 = \boldsymbol{u}^{4.0}_{\mathbf{lpf}}$	$(\boldsymbol{u})_0 = \boldsymbol{u}^{4.5}_{\mathbf{lpf}}$
Numb. Iters.	955	854	640	492	251
$\|\tilde{\boldsymbol{u}}^t - \boldsymbol{u}\|_{\text{fm}}$	37.17 %	37.01 %	37.03 %	36.84 %	36.91 %
avr($\|\mathbf{WSS}_{\mathbf{opt}}\|$)	2.83	2.85	2.85	2.87	2.88

Table 4: Results of optimised solutions (number of iterations, flow-matching norm and average WSS) for different initial guesses $\boldsymbol{u}_{\mathbf{snr}}$, $\boldsymbol{u}_0$, $\boldsymbol{u}^{3.5}_{\mathbf{lpf}}$, $\boldsymbol{u}^{4.0}_{\mathbf{lpf}}$ and $\boldsymbol{u}^{4.5}_{\mathbf{lpf}}$.

to the optimisation algorithm. However, the number of iterations to reach convergence was rather sensitive to this initial guess.

5.5. *Data assimilation for different Reynolds numbers*

In what follows, the measured and preprocessed data will now be denoted as $\boldsymbol{u}^{Re}_{\mathbf{snr}}$ representing the flow fields with different Re numbers, as described in section 5.1. Using the available data with increasing flow rates and setting the initial guesses to $\mathbf{0}$, algorithm 1 was executed with the input parameters $(\mathbf{0}, \boldsymbol{g}^{Re}_{\mathbf{snr}}, \boldsymbol{u}^{Re}_{\mathbf{snr}})$, where $\boldsymbol{g}^{Re}_{\mathbf{snr}} = \boldsymbol{u}^{Re}_{\mathbf{snr}}$ on Γ_i and $Re = \{\,1223, 1860, 2105, 4636, 7171\,\}$. The results are summarised in table 5. For considerate Re numbers, such as 1223, 1860 and 2105, it can be observed that the errors predicted by the classical CFD grow faster than the errors predicted by the optimisation strategy for increasing Re numbers. This confirms the feasibility of the proposed approach in comparison to traditional CFD methods. For higher Re numbers, such as 4636 and 7171, the model deficiency counteracts the role of the optimisation, yielding errors which are not to be considered seriously. However, the errors remain bounded, and are a clear indication that consideration of turbulence is a matter worth of research in the future.

$\boldsymbol{x} = \boldsymbol{u}_{\mathbf{snr}}^{Re}$	$\mathbf{nRMSE_2}(\boldsymbol{x}, \boldsymbol{y})$		$\mathbf{FDE_2}(\boldsymbol{x}, \boldsymbol{y})$	
Re	$\boldsymbol{y} = \boldsymbol{u}_{\mathbf{cfd}}$	$\boldsymbol{y} = \boldsymbol{u}_{\mathbf{opt}}$	$\boldsymbol{y} = \boldsymbol{u}_{\mathbf{cfd}}$	$\boldsymbol{y} = \boldsymbol{u}_{\mathbf{opt}}$
1223	51.72 %	48.78 %	0.41	0.48
1860	55.21 %	47.61 %	0.38	0.37
2105	63.32 %	48.36 %	0.39	0.42
4636	50.30 %	48.71 %	0.39	0.34
7171	55.41 %	56.98 %	0.41	0.37

Table 5: Root mean square errors ($\mathrm{nRMSE}_2(\boldsymbol{u}_{\mathbf{snr}}, \boldsymbol{y})$) and flow direction errors ($\mathrm{FDE}_2(\boldsymbol{u}_{\mathbf{snr}}, \boldsymbol{y})$) within the near-wall (2 mm) domain (E_2) for different Re numbers, where $\boldsymbol{y} = \{\, \boldsymbol{u}_{\mathbf{cfd}}, \boldsymbol{u}_{\mathbf{opt}} \,\}$.

6. Conclusion

In this work, an optimise-then-discretise approach was developed for the flow control problem using 4-D flow MRI data in the context of computational hemodynamics. The methodology was validated against an analytical solution as well as against experimental MR measurements performed in a glass replica of a human aorta.

The proposed control algorithm was analysed in detail in order to assess the capabilities of the methodology to reconstruct blood flow in near-wall regions, targeting the computation of hemodynamically relevant quantities such as the wall shear stress.

The method proved to deliver physically consistent flow fields with substantial reduction of noise present in the 4-D flow MRI measurements, outperforming the predictive capabilities of standard CFD approaches.

Overall, the flow control algorithm demonstrated robustness and feasibility towards reconstruction of flow fields from partial 4-D flow MRI measurements under different flow regimes with increasing Re numbers. Reconstruction of more complex flow structures observed in transient fluid dynamics and accounting for turbulence are out of the scope of the present work, and are matter of current research.

REFERENCES

Bhatia, H., Norgard, G., Pascucci, V. & Bremer, P. T. 2013 The Helmholtz-Hodge decomposition – a survey. *IEEE Trans. Vis. Comput. Graph.* **19** (8), 1386–1404.

Bouillot, P., Delattre, B. M., Brina, O., Ouared, R., Farhat, M., Chnafa, C., Steinman, D. A., K. O. Lovblad, V. M. Pereira & Vargas, M. I. 2017 3d phase contrast mri: Partial volume correction for robust blood flow quantification in small intracranial vessels. *Magn. Reson. Med.* .

Chatzizisis, Y. S., Coskun, A. Ü., Jonas, M., Edelman, E. R., Feldman, C. L. & Stone, P. H. 2007 Role of endothelial shear stress in the natural history of coronary atherosclerosis and vascular remodeling: molecular, cellular, and vascular behavior. *J. Am. Coll. Cardiol.* **49** (25), 2379–2393.

Chiu, J-J. & Chien, S. 2011 Effects of disturbed flow on vascular endothelium: Pathophysiological basis and clinical perspectives. *Physiol Rev.* **91** (1), 327–387.

Collis, S. S. & Heinkenschloss, M. 2002 Analysis of the Streamline Upwind/Petrov Galerkin Method Applied to the Solution of Optimal Control Problems. *Tech. Rep.* TR02–01. Department of Computational and Applied Mathematics, Rice University, Houston, TX 77005–1892.

Council, National Research 1991 *Four-Dimensional Model Assimilation of Data: A Strategy for the Earth System Sciences*. The National Academies Press.

D'Elia, M., Perego, M. & Veneziani, A. 2012 A variational data assimilation procedure for the incompressible navier-stokes equations in hemodynamics. *J. Sci. Comput.* **52** (2), 340–359.

D'Elia, M. & Veneziani, A. 2010*a* Methods for assimilating blood velocity measures in hemodynamics simulations: Preliminary results. *Procedia. Comput. Sci.* **1** (1), 1231–1239.

D'Elia, M. & Veneziani, A. 2010*b* A data assimilation technique for including noisy measurements of the velocity field into Navier-Stokes simulations. *Proc. of V European Conference on Computational Fluid Dynamics* .

Denaro, F. M. 2003 On the application of the Helmholtz-Hodge decomposition in projection methods for incompressible flows with general boundary conditions. *Int. J. Numer. Meth. Fluids* **3**, 43–69.

Garcia, D. 2011 A fast all-in-one method for automated post-processing of piv data. *Exp. Fluids* **50** (5), 1247–1259.

Gessner, F. B. 1973 Brief reviews: Hemodynamic theories of atherogenesis. *Circ. Research* **33** (3), 259–266.

Gudbjartsson, H. & Patz, S. 1995 The Rician distribution of noisy mri data. *Magn. Reson. Med.* **34** (6), 910–914.

Harouna, S. K. & Perrier, V. 2012 *Helmholtz-Hodge decomposition on* $[0,1]^d$ *by divergence-free and curl-free wavelets*, pp. 311–329. Springer Berlin Heidelberg.

Hochareon, P., Manning, K. B., Fontaine, A. A., Tarbell, J. M. & Deutsch, S. 2004 Wall shear-rate estimation within the 50cc penn state artificial heart using particle image velocimetry. *J. Biomech. Eng.* **126** (4), 430–437.

Ide, K., Courtier, P., Ghil, M. & Lorenc, A. C. 1997 Unified notation for data assimilation : Operational, sequential and variational. *J. Meteor. Soc. Japan.* **75** (1B), 181–189.

Johnson, H. J., McCormick, M., Ibáñez, L. & Consortium, The Insight Software 2013 *The ITK Software Guide*, 3rd edn. Kitware Inc.

Katritsis, D., Kaiktsis, L., Chaniotis, A., Pantos, J., Efstathopoulos, E. P. & Marmarelis, V. 2007 Wall shear stress: theoretical considerations and methods of measurement. *Prog. Cardiovasc. Dis.* **49** (5), 307–329.

Kolipaka, A., Illapani, V. S. P., Kalra, P., Garcia, J., Mo, X., Markl, M. & White, R. D. 2016 Quantification and comparison of 4d-flow mri-derived wall shear stress and mre-derived wall stiffness of the abdominal aorta. *J. Magn. Reson. Imaging* **45** (3), 771–778.

Ku, D. N., Giddens, D. P., Zarins, C. K. & Glagov, S. 1985 Pulsatile flow and atherosclerosis in the human carotid bifurcation. positive correlation between plaque location and low oscillating shear stress. *Arteriosclerosis.* **5** (3), 293–302.

Malek, A. M., Alper, S. L. & Izumo, S. 1999 Hemodynamic shear stress and its role in atherosclerosis. *JAMA-J. Am. Med. Assoc.* **282** (21), 2035–2042.

Markl, M., Frydrychowicz, A., Kozerke, S., Hope, M. & Wieben, O. 2012 4D flow MRI. *Magn. Reson. Im.* **36** (5), 1015–1036.

Patankar, S. V. & Spalding, D. B. 1972 A calculation procedure for heat, mass and momentum transfer in three-dimensional parabolic flows. *J. Heat Mass Transfer* **15**, 1787–1806.

Pelc, N. J., Herfkens, R. J., Shimakawa, A. & Enzmann, D. R. 1991 Phase contrast cine magnetic resonance imaging. *Magn. Reson. Q.* **7** (4), 229–254.

Raffel, M., Willert, C. E., Wereley, S. T. & Kompenhans, J. 2007 *Post-Processing of PIV Data*, pp. 177–208. Springer Berlin Heidelberg.

Reneman, R. S., Arts, T. & Hoeks, A. P. G. 2006 Wall shear stress–an important determinant of endothelial cell function and structure–in the arterial system in vivo. discrepancies with theory. *J. Vasc. Res.* **43** (3), 251–269.

Shaaban, A. M. & Duerinckx, A. J. 2000 Wall shear stress and early atherosclerosis: a review. *AJR Am. J. Roentgenol.* **174** (6), 1657–1665.

Texon, M., Imparato, A. M. & Helpern, M. 1965 The role of vascular dynamics in the development of atherosclerosis. *JAMA-J. Am. Med. Assoc.* **194** (11), 1226–1230.

Thang, C., Blatter, D. D. & Parker, D. L. 1995 Correction of partial-volume effects in phase-contrast flow measurements. *J. Magn. Reson. Imaging* **5** (2), 175–180.

Tiago, J., Guerra, T. & Sequeira, A. 2016 A velocity tracking approach for the data assimilation problem in blood flow simulations. *Int. J. Numer. Method Biomed. Eng.* .

Vorp, D. A. & Geest, J. P. Vande 2005 Biomechanical determinants of abdominal aortic aneurysm rupture. *Arterioscler Thromb Vasc Biol.* **25** (8), 1558–1566.

Vorp, D. A., Raghavan, M. L., Muluk, S. C., Makaroun, M. S., Steed, D. L., Shapiro, R. & Webster, M. W. 1996 Wall strength and stiffness of aneurysmal and nonaneurysmal abdominal aorta. *Ann. N. Y. Acad. Sci.* **800**, 274–276.

Walpola, P. L., Gotlieb, A. I. & Langille, B. L. 1993 Monocyte adhesion and changes in endothelial cell number, morphology, and f-actin distribution elicited by low shear stress in vivo. *Am J Pathol.* **142** (5), 1392–1400.

Weller, H. G., Tabor, G., Jasak, H. & Fureby, C. 1998 A tensorial approach to computational continuum mechanics using object-oriented techniques. *Comput. Phys.* **12** (6), 620–631.

Westerweel, J. & Scarano, F. 2005 Universal outlier detection for piv data. *Exp. Fluids* **39** (6), 1096–1100.

Yoshida, Y., Sue, W., Okano, M., Oyama, T., Yamane, T. & Mitsumata, M. 1990 The effects of augmented hemodynamic forces on the progression and topography of atherosclerotic plaques. *Ann. N. Y. Acad. Sci.* **598**, 256–273.

Zand, T., Majno, G., Nunnari, J. J., Hoffman, A. H., Savilonis, B. J., MacWilliams, B. & Joris, I. 1991 Lipid deposition and intimal stress and strain. a study in rats with aortic stenosis. *Am J Pathol.* **139** (1), 101–113.

Zarins, C. K., Zatina, M. A., Giddens, D. P., Ku, D. N. & Glagov, S. 1987 Shear stress regulation of artery lumen diameter in experimental atherogenesis. *J Vasc Surg.* **5** (3), 413–420.